

AD-A249 865



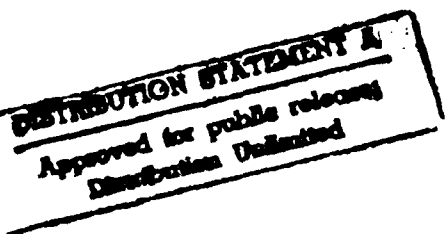
(2)



SSS-TR-91-12828

**Three-Dimensional Finite Difference Modeling
of Surface Wave Propagation
Across the Barents Shelf**

K. L. McLaughlin
T. G. Barker
J. L. Stevens
B. Shkoller
S. M. Day



Technical Report

**Sponsored by:
DEFENSE ADVANCED RESEARCH PROJECTS AGENCY (DoD)**

**Monitored by:
U.S. AIR FORCE TECHNICAL APPLICATIONS CENTER
Under Contract No. F08606-89-C-0022**

October 1991

**P. O. Box 1620, La Jolla, California 92038-1620
(619) 453-0060**

92-12434



92 5 08 032

REPORT DOCUMENTATION PAGE			Form Approved OMB No. 0704-0188
<p>Public reporting burden for this collection of information is estimated to average 1 hour per response, including the time for reviewing instructions, searching existing data sources, gathering and maintaining the data needed, and completing and reviewing the collection of information. Send comments regarding this burden estimate or any other aspect of this collection of information, including suggestions for reducing this burden, to Washington Headquarters Services, Directorate for Information Operations and Reports, 1215 Jefferson Davis Highway, Suite 1204, Arlington VA 22202-4302, and to the Office of Management and Budget, Paperwork Reduction Project (0704-0188), Washington, DC 20503.</p>			
1. AGENCY USE ONLY (Leave blank)	2. REPORT DATE October 1991	3. REPORT TYPE AND DATES COVERED Technical Report	
4. TITLE AND SUBTITLE Three-Dimensional Finite Difference Modeling of Surface Wave Propagation Across the Barents Shelf		5. FUNDING NUMBERS C - F08606-89-C-0022	
6. AUTHOR(S) K. L. McLaughlin, T. G. Barker, J. L. Stevens, B. Shkoller, and S. M. Day			
7. PERFORMING ORGANIZATION NAME(S) AND ADDRESS(ES) S-CUBED, A Division of Maxwell Laboratories, Inc. P.O. Box 1620 La Jolla, CA 92038-1620		8. PERFORMING ORGANIZATION REPORT NUMBER SSS-TR-91-12828	
9. SPONSORING/MONITORING AGENCY NAME(S) AND ADDRESS(ES) Defense Advanced Research Projects Agency 3701 N. Fairfax, Suite 717 Arlington, VA 22209-1714		10. SPONSORING/MONITORING AGENCY REPORT NUMBER	
11. SUPPLEMENTARY NOTES			
12a. DISTRIBUTION/AVAILABILITY STATEMENT Unlimited Distribution		12b. DISTRIBUTION CODE	
<p>13. ABSTRACT (Maximum 200 words)</p> <p>A three-dimensional (3D) finite difference simulation has been conducted of surface waves propagating across a laterally heterogeneous velocity and density model of the Barents Shelf. The 3D model encompasses a region of 1620 by 810 km to a depth of 210 km. The calculations were designed to model 0.02 to 0.05 Hz surface waves from an isotropic source at Novaya Zemlya in a 3D heterogeneous model.</p> <p>Extensive focusing/defocusing of surface waves are observed for the entire bandwidth from 0.02 to 0.05 Hz. Focusing/defocusing is observed to frequency dependent such that the amplitude patterns of 0.02 and 0.05 Hz are not correlated. A hybrid Fresnel-Kirchoff technique is used to project Rayleigh wave amplitudes to teleseismic distances. About 25 percent of the variance of the far-field Rayleigh wave amplitude scatter from Novaya Zemlya events can be explained by near-source (within 800 km) scattering.</p> <p>Multipathing was observed to occur for 0.04 to 0.05 Hz Rayleigh waves, consistent with observations of Novaya Zemlya events observed at the Norwegian Seismic Array (NORSAR). Rayleigh-to-Love conversion is observed in the simulation in localized regions along structural boundaries. Such scattered Love waves should be observable at narrow azimuthal ranges.</p>			
14. SUBJECT TERMS Surface Waves Finite Difference Barents Shelf		15. NUMBER OF PAGES 66	
		16. PRICE CODE	
17. SECURITY CLASSIFICATION OF REPORT Unclassified	18. SECURITY CLASSIFICATION OF THIS PAGE Unclassified	19. SECURITY CLASSIFICATION OF ABSTRACT Unclassified	20. LIMITATION OF ABSTRACT

UNCLASSIFIED

SECURITY CLASSIFICATION OF THIS PAGE

CLASSIFIED BY:

DECLASSIFY ON:

SECURITY CLASSIFICATION OF THIS PAGE

UNCLASSIFIED

TABLE OF CONTENTS

<u>SECTION</u>	<u>PAGE</u>
1. INTRODUCTION	1
2. OBSERVED LR PATH EFFECTS	3
3. TECTONIC RELEASE.....	7
4. THE MODEL	9
5. FINITE DIFFERENCE CALCULATIONS.....	20
6. ANALYSIS	21
7. TELESEISMIC LR AMPLITUDES.....	51
8. CONCLUSIONS AND DISCUSSION.....	56
9. ACKNOWLEDGEMENTS.....	58
10. REFERENCES	59

Accession For	
NTIS	GRA&I
DTIC TAB	<input type="checkbox"/>
Unannounced	<input type="checkbox"/>
Justification _____	
By _____	
Distribution/ _____	
Availability Codes	
Dist	Avail and/or
	Special

LIST OF ILLUSTRATIONS

<u>FIGURE</u>	<u>PAGE</u>
1 Novaya Zemlya long-period Rayleigh (LR) wave station corrections from Stevens and McLaughlin (1989)	4
2. The square of each station correction pair difference is normalized to the variance and plotted versus the station pair separation distance (BOTTOM).....	5
3. Inferred radiation patterns from four of the best recorded explosions at the northern Novaya Zemlya test site	8
4a Map of the Barents Sea region.	10
4b. Map of crustal thickness (Moho depth contours in km) of the Barents shelf region based on seismic and gravity data.....	11
4c. Map of granite-metamorphic layer (isopach contours in km) of the Barents shelf region based on seismic, gravity, and magnetic data.....	12
4d. Cross section across the Barents Shelf region derived from seismic and gravity data.....	13
5. Shear velocity contours on three sections, northwest (BOTTOM) west (MIDDLE), and southwest (TOP).....	14
6. Shear velocity models as a function of depth for 18 different regions of the 3D model separated into 5 distinct groups (see Figure 7).....	16
7. Phase velocities (TOP) and group velocities (BOTTOM) of 18 individual regions of the 3D model of the Novaya Zemlya - Barents Shelf area.....	17
8a. Contours of Rayleigh wave group velocity for the 3D model illustrate the complexity associated with the Barents Shelf sedimentary basins.....	18
8b. Shaded gray-scale contours of group Rayleigh wave velocity for the 3D model.....	19
9a. Snapshots (at 190 seconds) of the displacement field on the surface of the 3D finite difference grid.....	22

LIST OF ILLUSTRATIONS (Continued)

<u>FIGURE</u>	<u>PAGE</u>
9b. Snapshots (at 290 seconds) of the displacement field on the surface of the 3D finite difference grid.....	23
9c. Snapshots (at 350 seconds) of the displacement field on the surface of the 3D finite difference grid.....	24
10a. Vertical displacement seismogram section to the west (270 degrees).....	25
10b. Radial displacement seismogram section to the west (270 degrees).....	26
10c. Transverse displacement seismogram section to the west (270 degrees).....	27
11a. Vertical displacement seismogram section to the southwest (220 degrees).....	28
11b. Radial displacement seismogram section to the southwest (220 degrees).....	29
11c. Transverse displacement seismogram section to the southwest (220 degrees).....	30
12a. Contours of 25 second period peak vertical Rayleigh wave amplitudes with $1/\sqrt{R}$ geometrical spreading correction on the surface of the 3D grid.....	32
12b. Contours of 30 second period peak vertical Rayleigh wave amplitude on the surface of the 3D grid.....	33
12c. Contours of 40 second period peak vertical Rayleigh wave amplitude on the surface of the 3D grid.....	34
12d. Contours of 50 second period peak vertical Rayleigh wave amplitude on the surface of the 3D grid.....	35
13a. Contours of 25 second period peak radial amplitudes with $1/\sqrt{R}$ geometrical spreading correction on the surface of the 3D grid.....	36

LIST OF ILLUSTRATIONS (Continued)

<u>FIGURE</u>	<u>PAGE</u>
13b. Contours of 40 second period peak radial amplitudes with $1/\sqrt{R}$ geometrical spreading correction on the surface of the 3D grid	37
14a. Contours of 25 second period peak transverse amplitudes with $1/\sqrt{R}$ geometrical spreading correction on the surface of the 3D grid	38
14b. Contours of 40 second period peak transverse amplitudes with $1/\sqrt{R}$ geometrical spreading correction on the surface of the 3D grid	39
15a. Contours of the ratio of Transverse/Radial 25 second period motion on the surface of the 3D grid.....	40
15b. Contours of the ratio of Transverse/Radial 40 second period motion on the surface of the 3D grid.....	41
16a. Group delay contours for 25 second period vertical Rayleigh waves on the surface of the 3D grid. Contours show wave energy refracting around the Barents Shelf sedimentary basins to the southwest of the source.....	42
16b. Group delay contours for 30 second period vertical Rayleigh waves on the surface of the 3D grid.....	43
16c. Group delay contours for 40 second period vertical Rayleigh waves on the surface of the 3D grid.....	44
16d. Group delay contours for 50 second period vertical Rayleigh waves on the surface of the 3D grid.....	45
17a. Phase delay contours for 25 second period vertical Rayleigh waves on the surface of the 3D grid.....	46
17b. Inferred phase velocity contours for 25 second period vertical Rayleigh waves on the surface of the 3D grid.....	47
18a. Broadband (0.04-0.05 Hz) frequency-wavenumber (f-k) analysis of radial (upper left), vertical (upper right), and transverse (lower left) component motion from a 25 station array in the southwest corner of the grid.....	49

LIST OF ILLUSTRATIONS (Continued)

<u>FIGURE</u>	<u>PAGE</u>
18b. Broadband (0.04 - 0.05 Hz) frequency-wavenumber (f-k) analysis of radial (upper left), vertical (upper right), and transverse (lower left) component motion from a 25 station array.....	50
19a. Predicted Fresnel-Kirchoff amplitudes for teleseismic Rayleigh waves in several bandwidths	52
19b. Perspective mesh of the predicted Fresnel-Kirchoff amplitudes for teleseismic Rayleigh waves as a function azimuth from the source (190-370 degrees) and frequency (0.02-0.05 Hz).....	53
19c. Predicted Fresnel-Kirchoff amplitudes for 0.02-0.05 Hz teleseismic Rayleigh waves assuming two ranges in phase velocity, 3.5-3.7 and 3.8-4.0 km/s	54

ABSTRACT

A three-dimensional (3D) finite difference simulation has been conducted of surface waves propagating across a laterally heterogeneous velocity and density model of the Barents Shelf. The 3D model encompasses a region of 1620 by 810 km to a depth of 210 km. The calculations were designed to model 0.02 to 0.05 Hz surface waves from an isotropic source at Novaya Zemlya in a 3D heterogeneous model.

Extensive focusing/defocusing of surface waves are observed for the entire bandwidth from 0.02 to 0.05 Hz. Focusing/defocusing is observed to be frequency dependent such that the amplitude patterns of 0.02 and 0.05 Hz are not correlated. A hybrid Fresnel-Kirchoff technique is used to project Rayleigh wave amplitudes to teleseismic distances. About 25 percent of the variance of the far-field Rayleigh wave amplitude scatter from Novaya Zemlya events can be explained by near-source (within 800 km) scattering.

Multipathing was observed to occur for 0.04 to 0.05 Hz Rayleigh waves, consistent with observations of Novaya Zemlya events observed at NORSAR. Rayleigh-to-Love conversion is observed in the simulation in localized regions along structural boundaries. Such scattered Love waves should be observable at narrow azimuthal ranges.

1. INTRODUCTION

Surface waves from Novaya Zemlya encounter substantial 3D lateral heterogeneity as they propagate in the first several hundred kilometers. The transition from thickened continental crust to shelf, ocean, and shield in the vicinity of Novaya Zemlya is particularly complex. The complexity of the region is evident in the LR multipathing observed by Levshin and Berteussen (1979) for Rayleigh waves arriving at NORSAR from Novaya Zemlya across the mixed Barents Shelf and Fennoscandia shield path. The Barents Shelf to the west of Novaya Zemlya has deep sedimentary basins that are responsible for anomalously slow group velocities for 20 to 30 second waves as observed in northern Fennoscandia (Levshin and Berteussen, 1979; and Chan and Mitchell, 1985). Propagation to the northwest must cross oceanic crust with thick sedimentary cover and then back to continental crust in the vicinity of Spitsbergen and Franz Josef Land. For propagation paths to Europe, Greenland, and North America the surface waves must propagate obliquely across various portions of these structures. Zeng, *et al.*, (1989) have demonstrated that the focusing-defocusing by these near-source structures and other lateral variations in the Arctic Ocean produce substantial variations in surface wave amplitude across North America.

In previous work McLaughlin, *et al.*, (1991) modeled near source scattering of surface waves by lateral variations surrounding the Amchitka Island Test Site in the Aleutian islands. It was demonstrated that both lateral refraction and Rayleigh to Love conversion was possible in the presence of shallow heterogeneity typical of a subduction zone. In this paper we simulate the propagation of surface waves through structure within 800 km of Novaya Zemlya using these same methods. A 3D velocity and density model is constructed based on regional geologic models from the literature. Then 3D elasto-dynamic finite-difference calculations are used to simulate the complete seismic-wavefield from an isotropic source in the 3D laterally heterogeneous model. The simulations are then analyzed for implications on the propagation of surface waves from Novaya Zemlya across the Barents shelf.

We find that laterally heterogeneous structure in the Barents Shelf region west of Novaya Zemlya is sufficient to introduce far-field focusing/defocusing,

multipathing, and Rayleigh to Love conversion in the 0.02 to 0.05 Hz bandwidth consistent with observations. These 3D finite difference simulations provide insights into the LR scattering mechanisms and provide estimates for magnitude variations that can be introduced by strong crustal contrasts in the vicinity of the source. These scattering effects are significant even for 50 second period Rayleigh waves.

2. OBSERVED LR PATH EFFECTS

LR log-amplitudes from explosions are typically scattered with standard deviations in the range of 0.2 to 0.3 log-units. Even when systematic source-receiver path corrections are taken into account, moment: m_b , and/or moment:log-yield regressions reveal that considerable scatter remains in the excitation and propagation of long-period seismic energy. Both the uncertainty in path corrections and the presence of tectonic release contribute to this scatter. We briefly examine data from the northern Novaya Zemlya test site to illustrate the nature of this scatter. First we examine path effects alone and then the evidence for tectonic release.

Figure 1 shows 86 station corrections with estimated standard errors inferred from a suite of 19 northern Novaya Zemlya explosions by Stevens and McLaughlin (1988). The explosions are assumed to be isotropic and after spectral Rayleigh wave amplitudes are corrected for path dispersion and attenuation (see Stevens, 1986), station corrections are derived from the station log-moment residuals with respect to the network average. These log-moment station corrections have a range of 1.03 (factor of 10.7) and a standard deviation (σ) of 0.218 (factor of 1.65) and represent 76% of the total variance in Rayleigh wave log-moment scatter seen from Novaya Zemlya in the 0.02 to 0.05 Hz bandwidth.

The station corrections are shown plotted in Figure 1 as a function of azimuth from 0 to 360 degrees as well as an expanded plot from 315 to 360 degrees. On initial inspection the station corrections appear to be nearly random, with little or no azimuthal pattern. However, groups of stations spaced within a few degrees of each other in azimuth show consistent variation. This deterministic azimuthally dependent path effect is clearly apparent for stations in the northwest quadrant (315 to 360 degrees). Within the estimated error bars the station corrections exhibit a smooth variation in amplitude variation.

To quantify this correlation between adjacent stations, we plot a smoothed variogram and the inferred correlation function in Figure 2. The variogram is a plot of the squared differences between pairs of station corrections plotted against the separation in azimuth between the stations. The

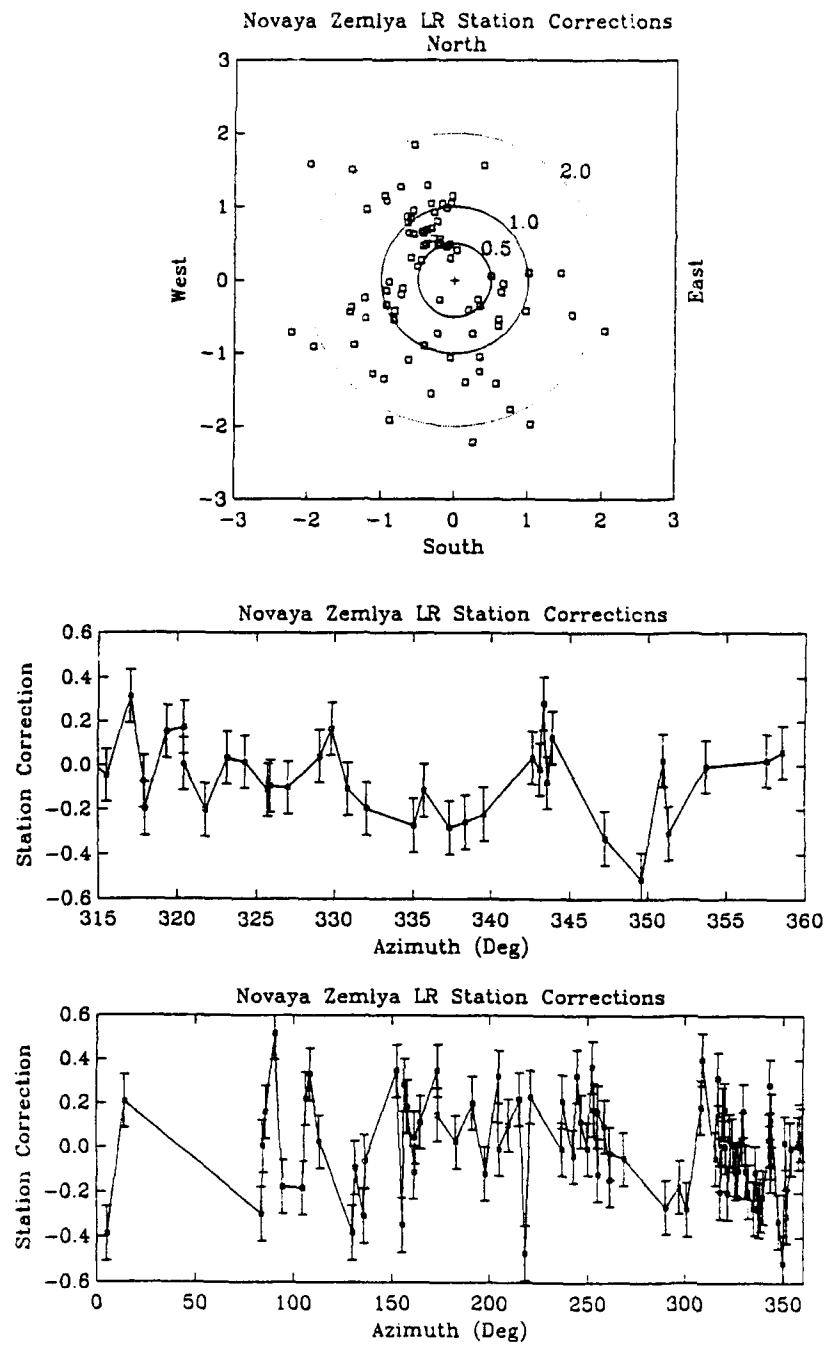


Figure 1. Novaya Zemlya long-period Rayleigh (LR) wave station corrections from Stevens and McLaughlin (1989). Station corrections (log-amplitude) and estimated standard errors are plotted at a function of station azimuth from 0 to 360 degrees (BOTTOM). The azimuth range from 315 to 360 degrees is shown at a larger scale (MIDDLE). Amplitude factors are plotted in a polar format at the azimuth of the station from the source (TOP).

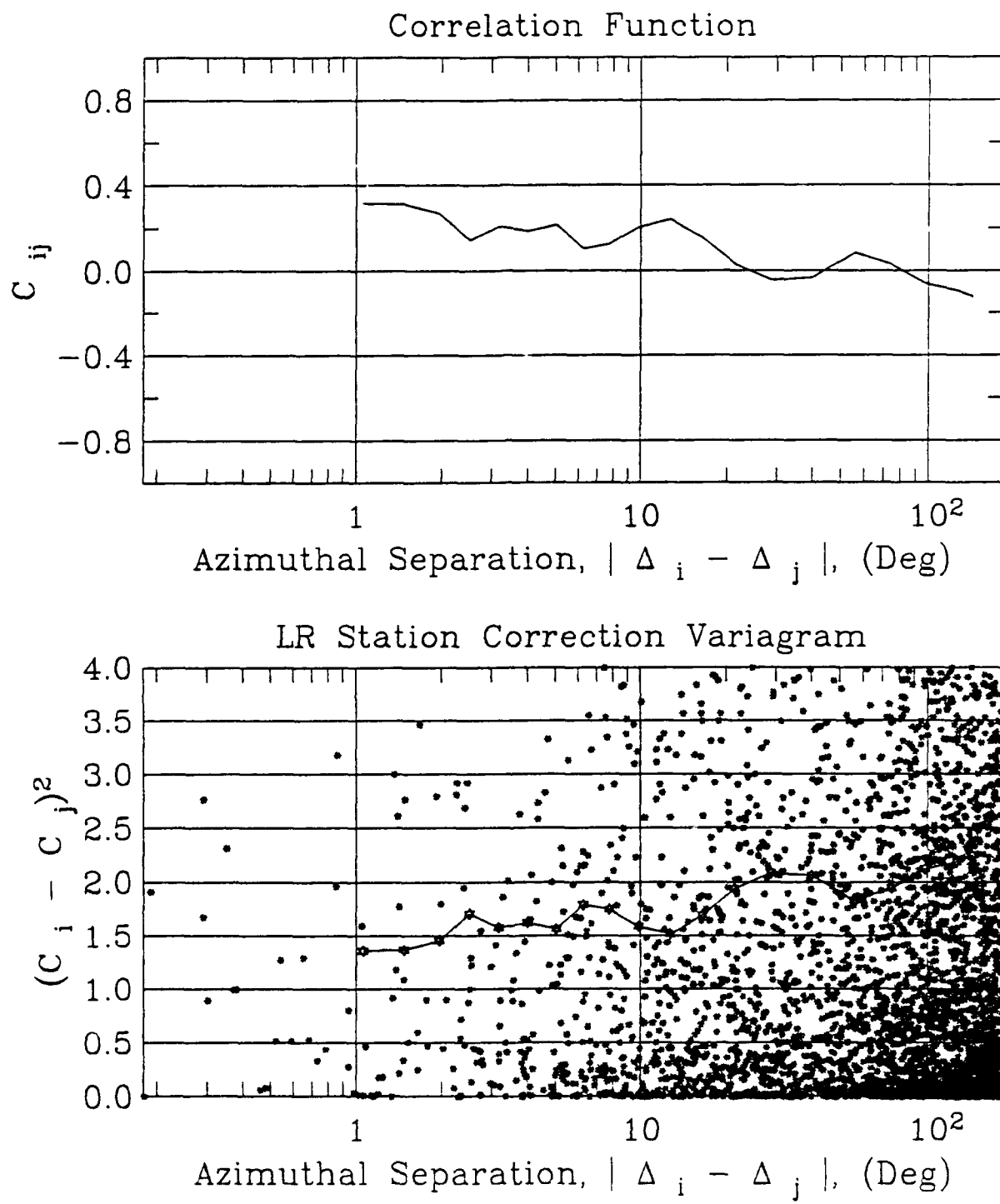


Figure 2. The square of the each station correction pair difference is normalized to the variance and plotted versus the station pair separation distance (BOTTOM). The inferred correlation function (TOP) is derived from the smoothed variogram (BOTTOM).

variation between stations is normalized to the variance of the distribution, $V_{ij} = (c_i - c_j)^2 / \sigma^2$, where c_i is the i 'th station correction. If the individual station corrections are random and independent then the variation should average to 2. If the station corrections are correlated then the average variation will be less than 2. If two stations are close together, $|\theta_i - \theta_j| < 10$ degrees, the average variation is significantly less than 2, suggesting a valid correlation. The inferred correlation function, $C_{ij}(\delta\theta_{ij}) = 1 - \frac{1}{2} V_{ij}$, inferred from the smoothed variogram is shown in the upper panel of Figure 2. For pairs of stations located within two degrees in azimuth of each other, the station corrections are 30% correlated. The correlation function decays for increasing distance to nearly zero for station pairs separated in azimuth by more than 10 degrees suggesting that they are independent.

We therefore conclude that 30% of the variance (randomness) in the station corrections is due to deterministic path effects that vary in azimuth across the network with characteristic lengths of about 10 degrees. Since there are many gaps in network coverage, the deterministic pattern is aliased for most azimuths. This deterministic pattern represents 30% of the total observed variance or an rms variation of 0.12 (factor of 1.32) in log-moment station corrections. Because deterministic patterns in the station corrections could be due to non-isotropic radiation as well as source-receiver path effects we need to look at the possibility that the station corrections contain tectonic release information.

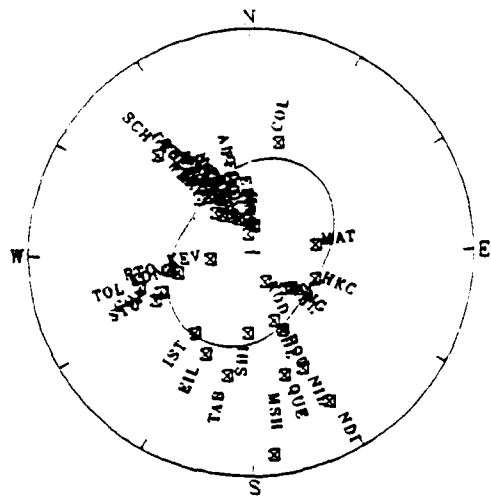
3. TECTONIC RELEASE

Tectonic release at the Novaya Zemlya test site has been investigated by Tucker, *et al.* (1989, 1990), Stevens and McLaughlin (1988), Burger, *et al.* (1986), and others. Figure 3 shows the result of moment tensor inversion of the Rayleigh wave amplitudes of four northern Novaya Zemlya explosions. Two of these explosions have a very small amount of tectonic release. In fact, given the amount of scatter in the data, the tectonic component of these explosions is not significantly different from zero. Only one of these events (1973255), has a significant amount of tectonic release. These moment tensor inversions were performed without station corrections, and as is evident from the figures, the amount of scatter remaining after the tectonic contamination is removed is substantial.

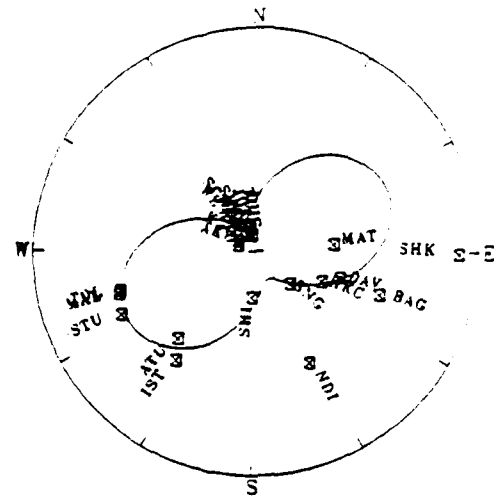
Although tectonic release is present in some events, the largest contributor to the total variance in log-moment is path related. From the analysis described in the previous section, we find that 70 percent of the station correction variance is uncorrelated for station separations greater than 10 degrees, and station corrections account for 76 percent of the total variance of a population of 19 events.

1970287

1973255



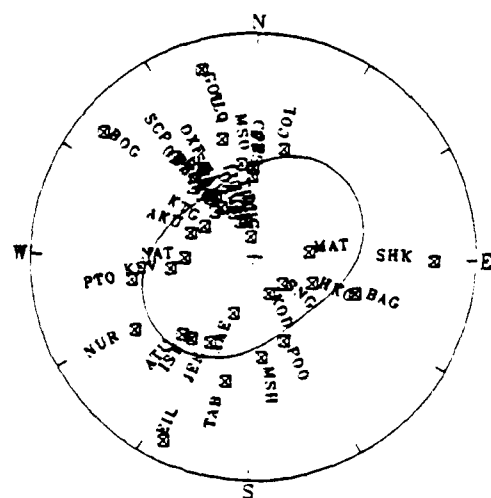
$f = 0.11$, strike = 348.629, $M_i = 7.997E + 16$



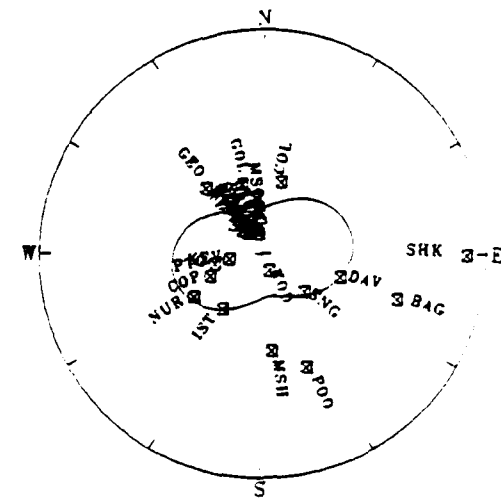
$f = 0.38$, strike = 18.570, $M_i = 1.965E + 17$

1974241

1975235



$f = 0.12$, strike = 6.882, $M_i = 8.634E + 16$



$f = 0.21$, strike = 34.558, $M_i = 4.817E + 16$

Figure 3. Inferred radiation patterns from four of the best recorded explosions at the northern Novaya Zemlya test site. No station corrections are used prior to inversion for tectonic release. No significant non-isotropic component to the radiation pattern is statistically significant except for event 1973255, when station corrections are applied prior to inversion for tectonic release.

4. THE MODEL

We see from far-field surface wave amplitude data that there is evidence for both tectonic release and source-receiver path effects. In order to examine propagation effects of 3D structure within 800 km of the Novaya Zemlya test site, we have constructed a 3D velocity and density model based on regional geologic models and then conducted a 3D finite difference simulation of surface wave propagation.

The velocity and density model for the Novaya Zemlya, Barents shelf, Kola peninsula region was based on data from Clarke and Rachlin (1990) which was compiled from the geologic modeling and deep seismic sounding literature. Figures 4b and 4c show contours of crustal thickness, granitic layer isopachs, regions of missing granitic layer, and regions of reduced sedimentary cover. The Barents shelf is a region of continental crust that has undergone considerable extension and thinning. The basins have filled in places with as much as 20 km of sediments. The Barents Sea is bounded to the east by Novaya Zemlya, to the north by the Svalbard platform, Spitsbergen, and Franz Josef Land, to the southwest by the Kola and Kanin Peninsulas, and to the south by the Pechora Basin. Novaya Zemlya is considered an extension of the Ural fold belt and is a region of thick crustal thickness (40-50 km). The Kola peninsula is an old shield area of thick (40 km) crust and reduced sedimentary cover. Similarly, the Svalbard platform and regions around Spitsbergen and Franz Josef Land to the north are continental crust (40 km). The Pechora Basin between the Ural fold belt and the Kanin peninsula has a reduced crustal thickness (< 35 km) and is related to the extensional features of the Barents shelf.

From this general geologic model a 3D seismic velocity model was derived for the region. Velocities and densities for the sediments, "granite layer," "basaltic layer," and mantle were each given a depth dependence consistent with the velocity section shown in Figure 4d adapted from Clarke and Rachlin. The 3D velocity model was sampled on a grid at 5 km intervals in depth and at 50 km intervals in north-south and east-west directions. For the purposes of calculation, the model was discretized as 6 by 6 by 6 km cells. Cross sections of the velocity model are shown in Figure 5. The results of this model generation

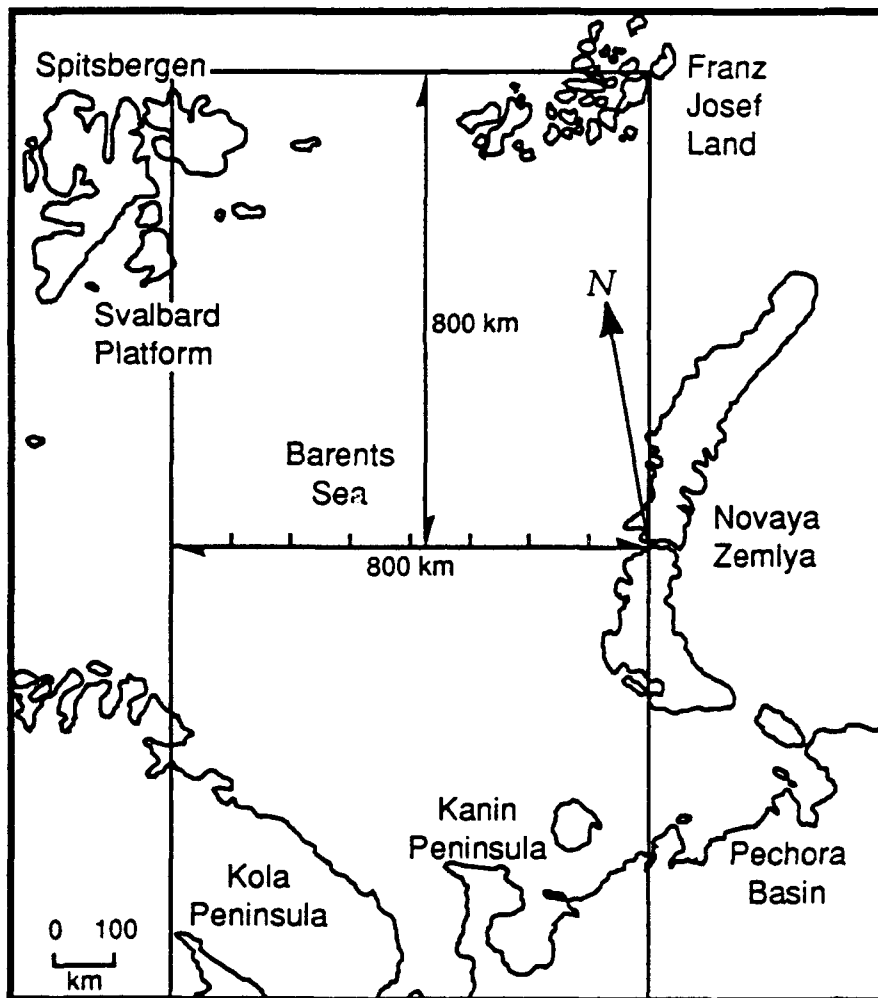


Figure 4a Map of the Barents Sea region. The 3D finite difference grid modeled long-period wave propagation in a rectangular region 1620 km by 810 km around the northern Novaya Zemlya test site.

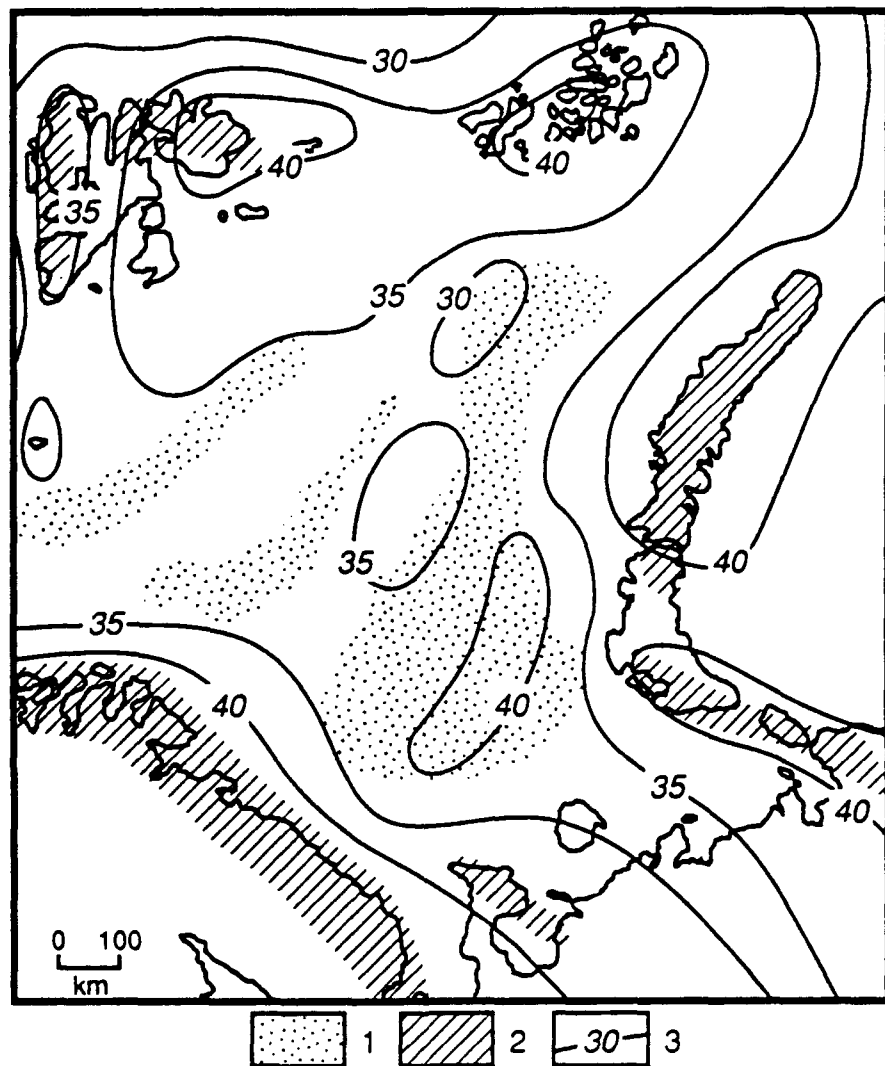


Figure 4b. Map of crustal thickness (Moho depth contours in km) of the Barents shelf region based on seismic and gravity data. Stippled areas are regions of missing granitic crust. Hatched areas are regions of reduced sedimentary cover. Adapted from Clarke and Rachlin (1990).

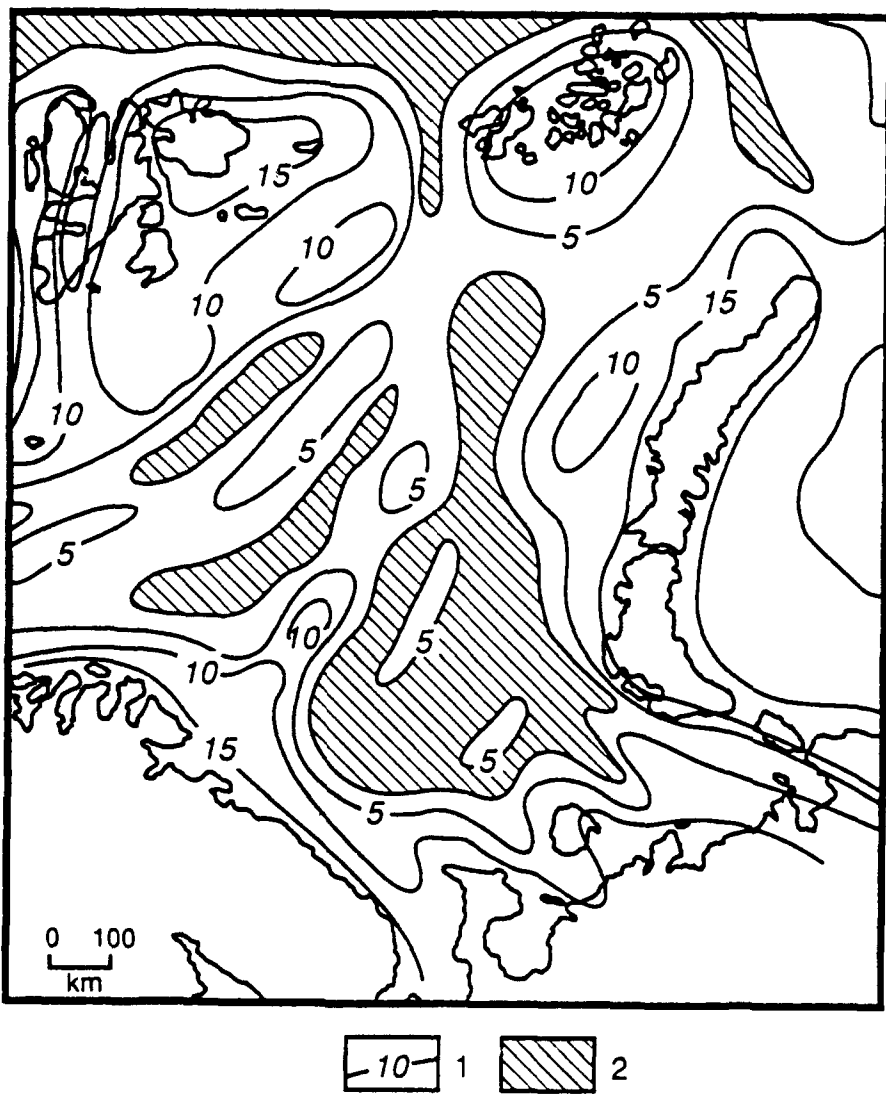


Figure 4c. Map of granite-metamorphic layer (isopach contours in km) of the Barents shelf region based on seismic, gravity, and magnetic data. Hatched areas are regions of missing granite-metamorphic layer inferred from magnetic data. Adapted from Clarke and Rachlin (1990).

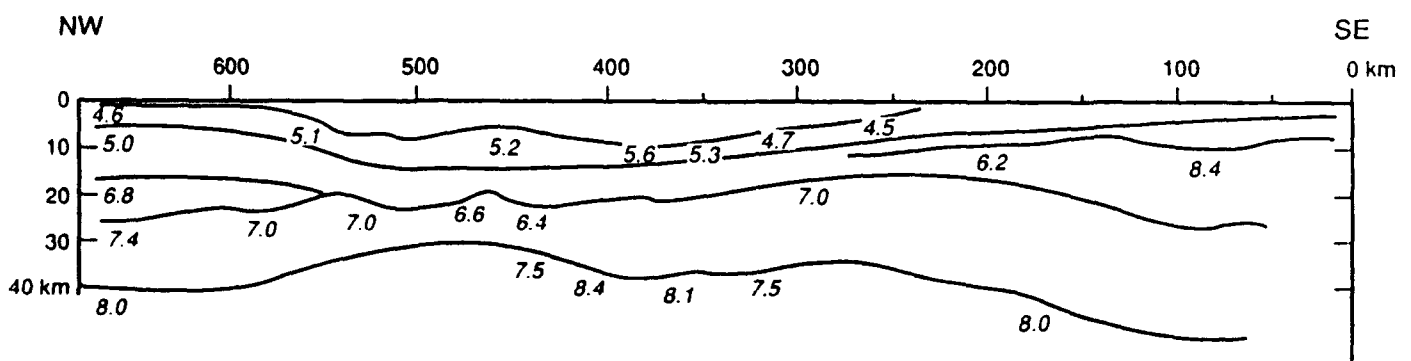


Figure 4d. Cross section across the Barents Shelf region derived from seismic and gravity data. Adapted from Clarke and Rachlin (1990).

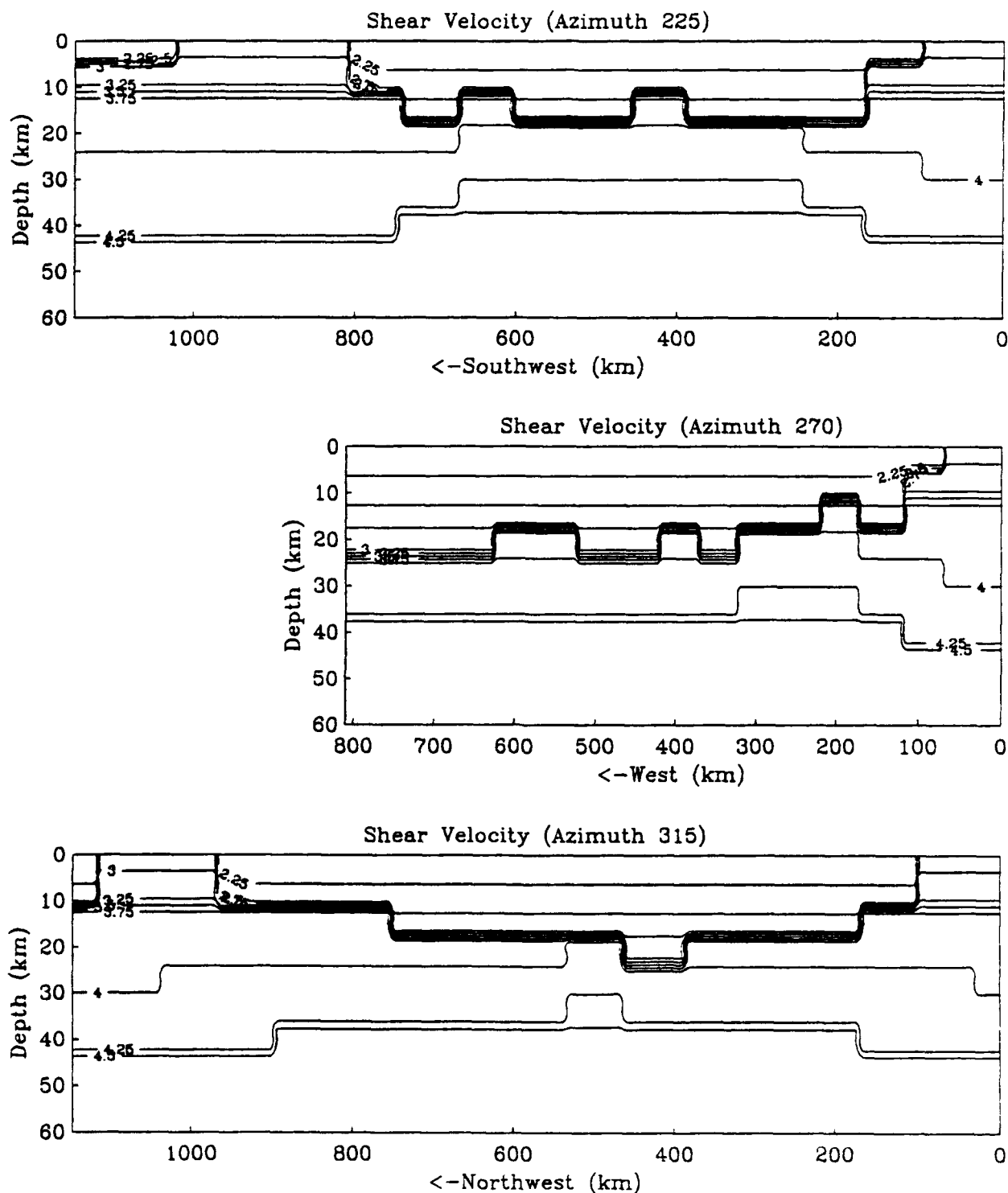


Figure 5. Shear velocity contours on three sections, northwest (BOTTOM), west (MIDDLE), and southwest (TOP).

was a pastiche of 18 different crustal and upper mantle velocity models arranged on a grid (see Figure 6). Phase and group velocities for these 18 different crustal models are shown in Figure 7 to demonstrate that they fall into roughly five different sets of dispersion curves corresponding to shield, shield with sediment cover, shallow sedimentary basin, deep sedimentary basin, and oceanic models. Figures 8a and 8b show fundamental Rayleigh wave group velocities for several frequencies contoured on the surface of the model grid. The low velocity basins are clear features at all frequencies but most dominant at the higher frequencies (0.05 Hz).

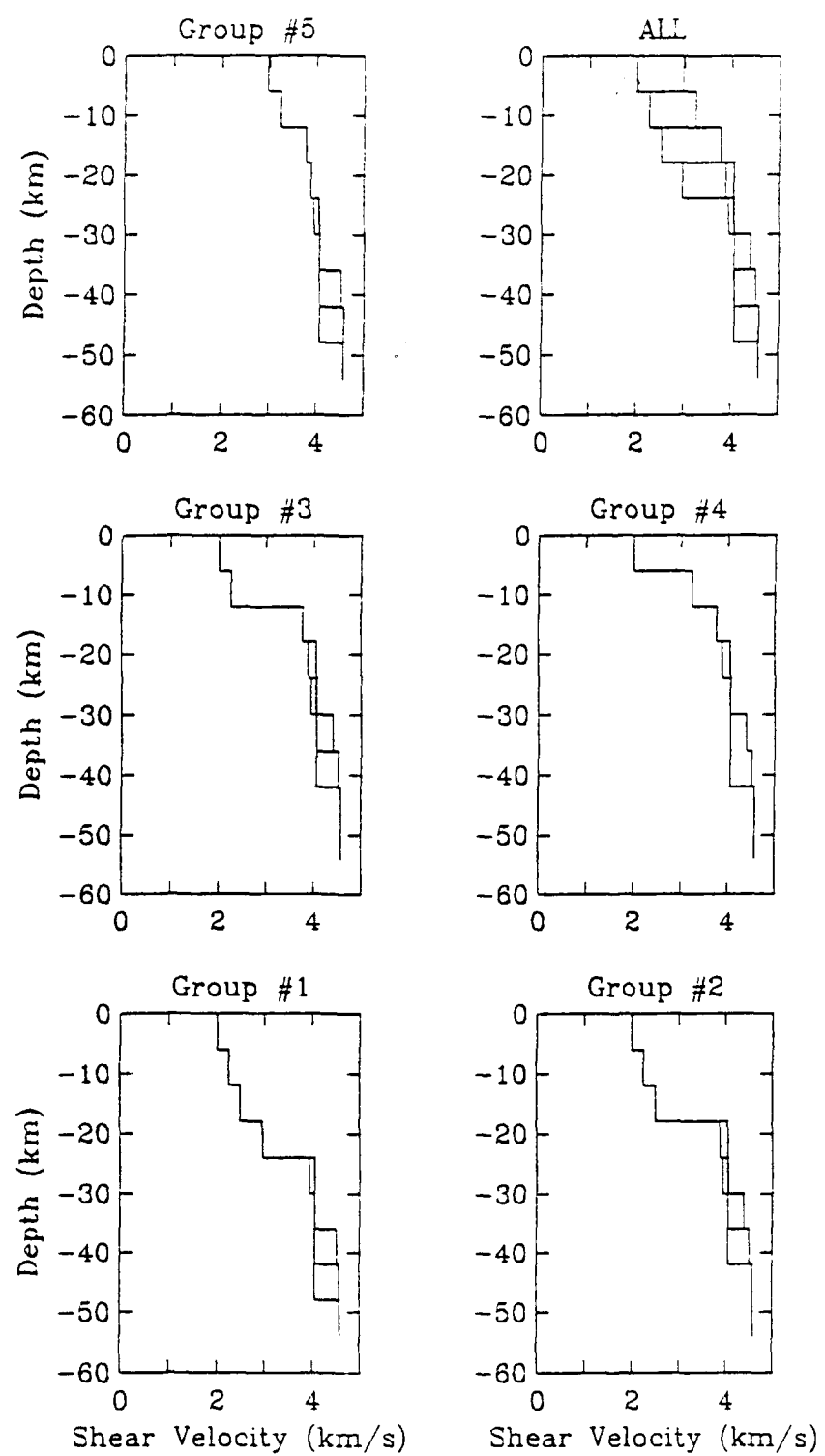


Figure 6. Shear velocity models as a function of depth for 18 different regions of the 3D model separated into 5 distinct groups (see Figure 7).

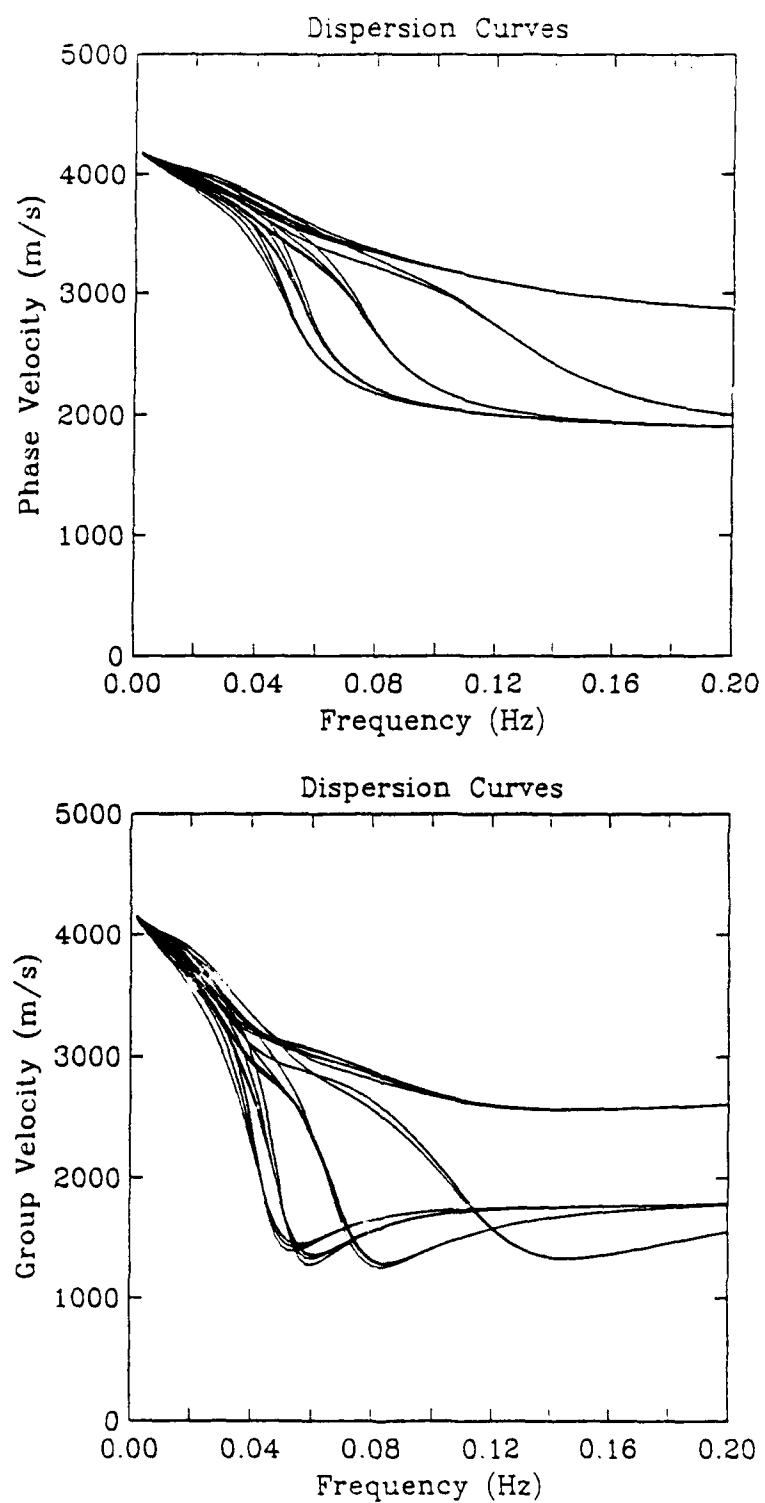


Figure 7. Phase velocities (TOP) and group velocities (BOTTOM) of 18 individual regions of the 3D model of the Novaya Zemlya - Barents Shelf area. The 18 regions cluster into 5 distinct groups.

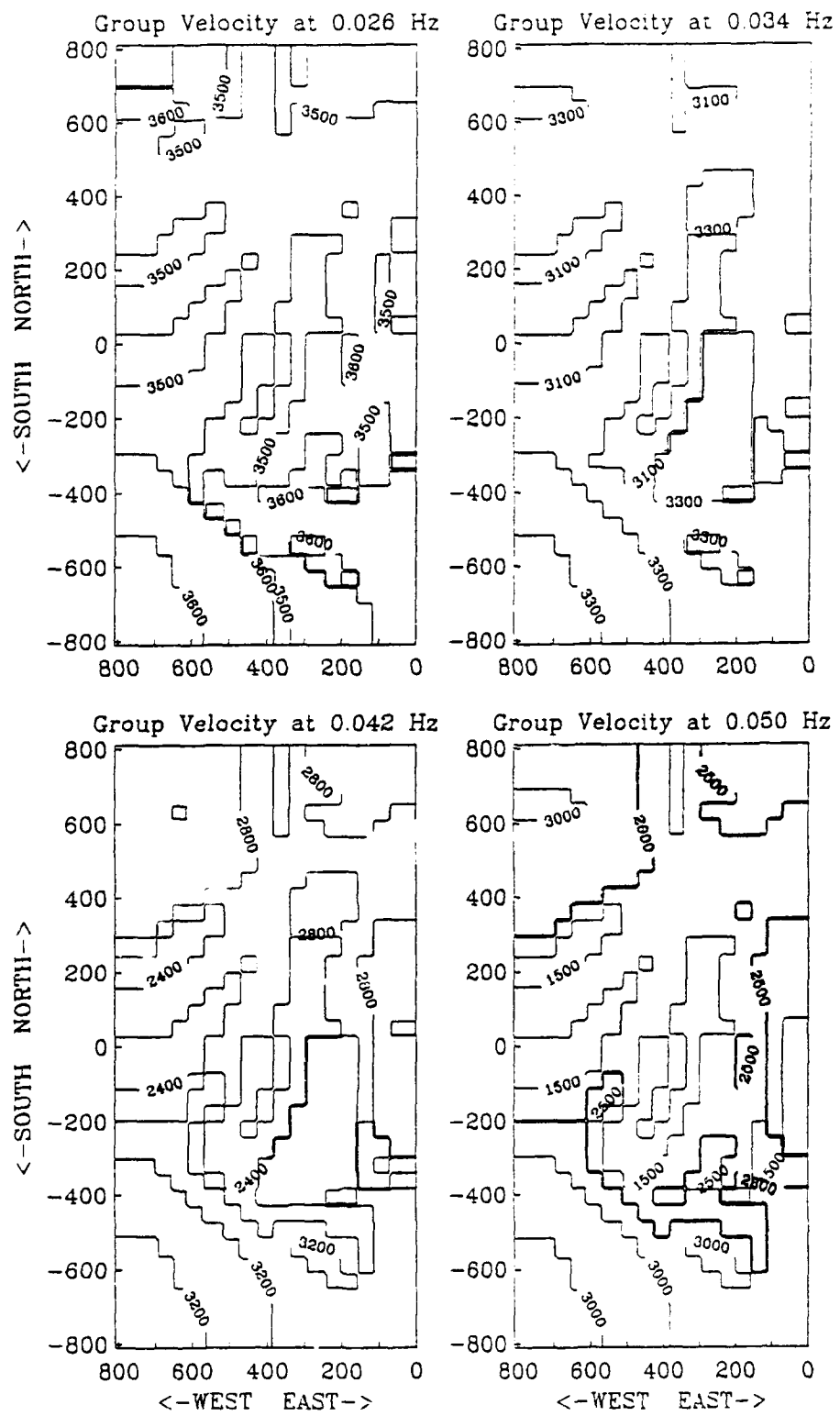
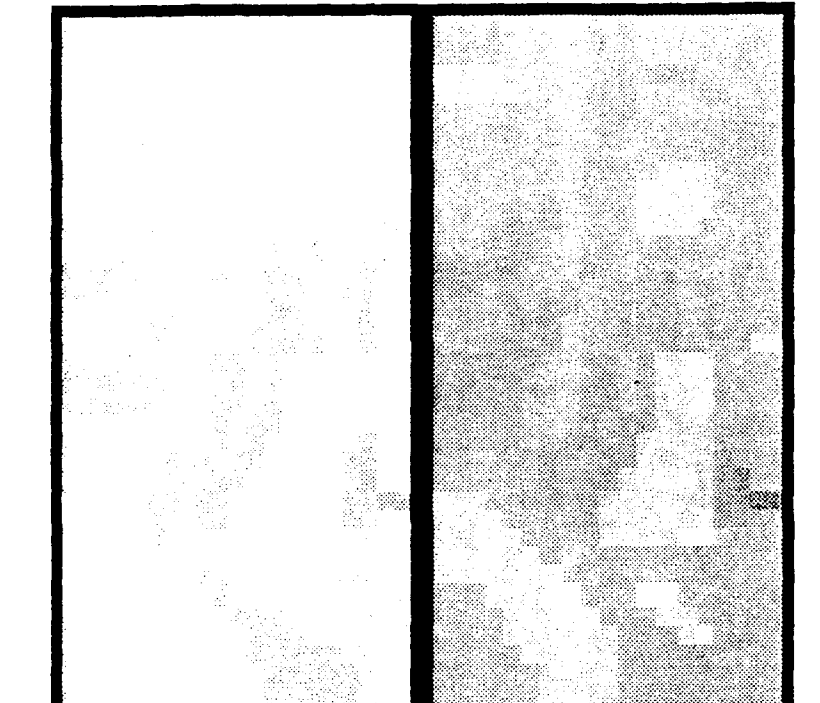


Figure 8a. Contours of Rayleigh wave group velocity for the 3D model illustrate the complexity associated with the Barents Shelf sedimentary basins.

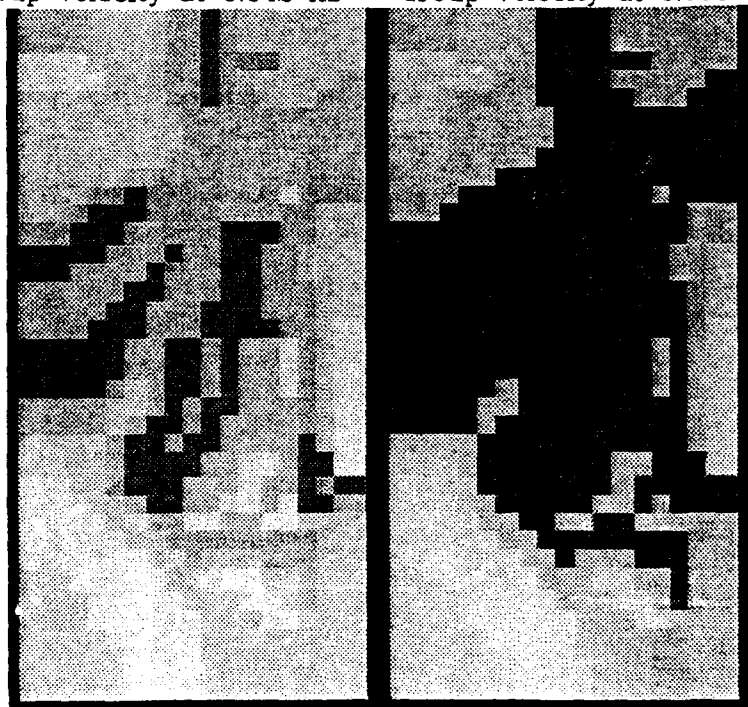
Group Velocity at 0.026 Hz Group Velocity at 0.034 Hz

<- SOUTH NORTH ->



Group Velocity at 0.042 Hz

<- SOUTH NORTH ->



<- WEST EAST ->

<- WEST EAST ->

Figure 8b. Shaded gray-scale contours of group Rayleigh wave velocity for the 3D model. Note the increase in complexity and contrast in the group velocity structure for the higher frequencies.

5. FINITE DIFFERENCE CALCULATIONS

The computational grid was designed to model 20 to 50 second surface waves from an isotropic explosion in a laterally heterogeneous structure. The 6 km cell size ensured that the shortest shear wavelengths of interest were longer than 8 to 10 cells. The useful model as indicated in Figure 4a is a grid of 270 by 135 by 35 cells (1620 km north-south, 810 km east-west, and 210 km vertical). Experience gained from similar calculations (McLaughlin, et al., 1991) showed that a 200 km deep grid was adequate to propagate 20 to 50 second period surface waves. An east-west reflection symmetry was assumed for the velocity model across a north-south line through the source so the effective useful model was 1620 by 1620 by 210 km. Outside the useful model to the north, south, west, and at depth were buffer regions, 15 cells thick. The cell sizes in these buffer regions increase at a compounding rate of 5% outside the useful model region to place the grid boundaries farther from the useful grid than would be possible with a grid of constant cell size. Artificial viscosity is used to damp reflections from the regions of expanding grid and reflections from the grid boundaries to the north, south, west, and at depth. Therefore, the total computational grid was 301 by 151 by 51 for a total of 2.318 million cells. The elastodynamic finite difference equations were integrated with a time step (cycle) of 0.25 seconds for a total of 500 seconds (total of 4.6 billion cell-cycles). The fully vectorized computation using the TRES 3D finite difference code required approximately 3 hours of CPU time on a 256 million word CRAY 2.

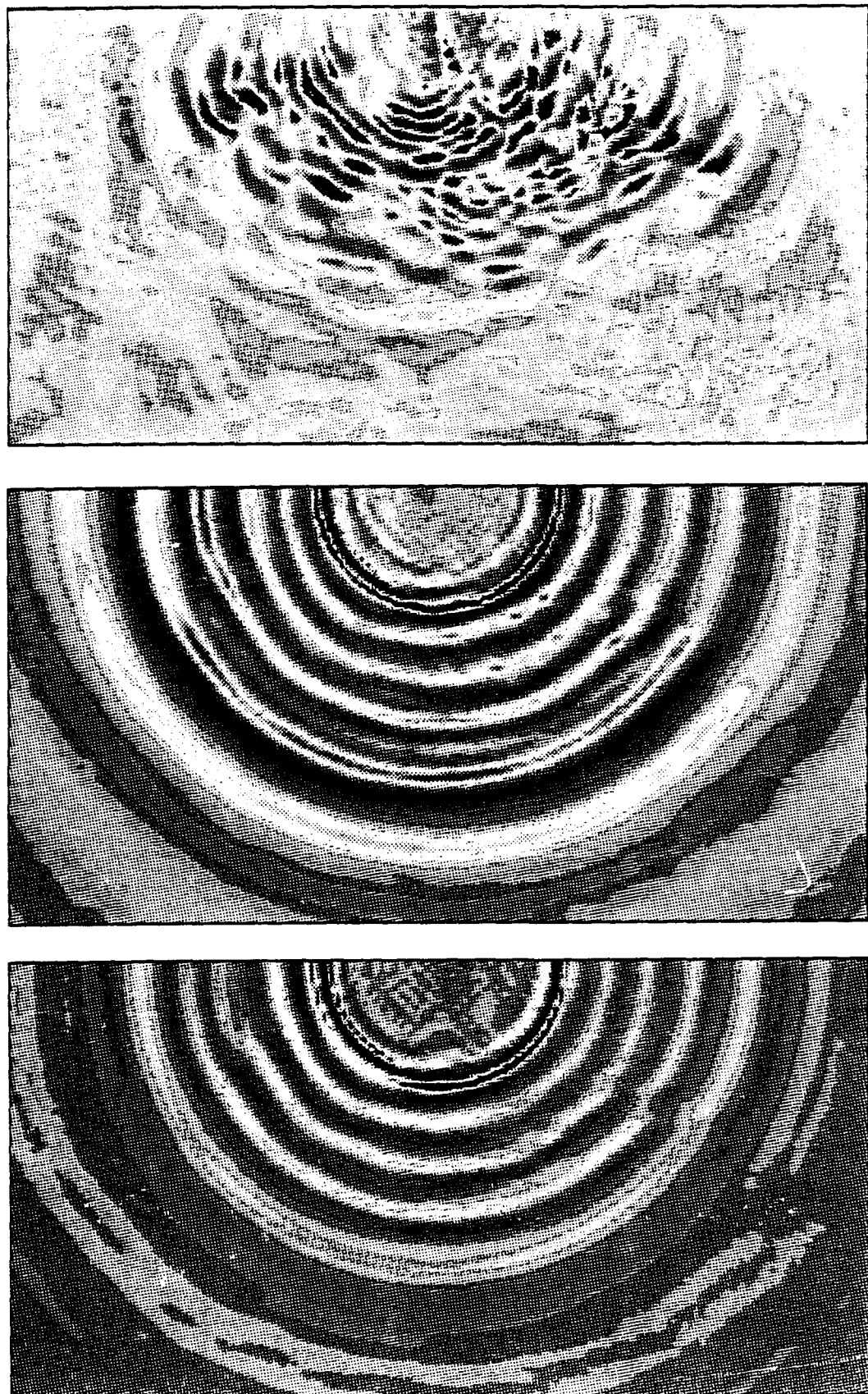
An explosion source is introduced as an isotropic moment tensor with a time function proportional to $\alpha^2 t e^{-\alpha t}$ and $\alpha = 0.1$ Hz. This is a minimum-phase source time function with a corner frequency of 0.1 Hz and high-frequency roll-off proportional to ω^{-2} . In this manner the simulation is dominated by the low-frequency bandwidth of interest and snap-shots (or movies) of the displacement field (surface waves) can be visualized without post-processing. Displacements were saved for every fourth time step on the surface of the grid ($z=0$) and on vertical planes passing through the source in the north-south ($x=0$) and east-west ($y=0$) directions. The analysis of these displacement fields is presented in the next section.

6. ANALYSIS

The displacement seismograms saved on the surface of the 3D grid at 12 km intervals serve as a basis for our analysis of the surface wave propagation in the 3D grid. Snapshots of the displacement field on the surface of the 3D finite difference grid are shown for 190, 290 and 350 seconds in Figures 9a-c. The vertical (Z) and radial (R) components of motion show development of asymmetrical Rayleigh wave propagation while the transverse (T) component shows developing Love wave coda. Rayleigh to Love conversion is most prominent along the edges of the sedimentary basins where the Rayleigh waves must propagate at oblique angles to the structural contrasts. Focusing by the low-velocity sedimentary basins is clearly evident on the vertical and radial components of motion. Furthermore, the dispersed wavefronts are distorted as they refract around the low velocity basins and are delayed across the basins. This is clearly visible in the wavefield to the southwest and northwest of the source.

In order to more fully understand these wave phenomena we have processed the displacement seismograms on the surface of the grid using standard surface wave processing algorithms. Narrow band filters are applied at selected frequencies and the peak amplitude, phase, and group delay of the Rayleigh wave is estimated. In the following analysis we present the results for 25, 30, 40, and 50 second vertical component Rayleigh waves.

Seismograms along sections to the west and southwest are shown in Figures 10a,b,c and 11a,b,c. The vertical and radial displacement waveforms show a Pn-Pg wavefield followed by the much larger dispersed fundamental Rayleigh wavetrain. Vertical and radial motion are fairly coherent with each other while the transverse component has a weak Pn-Pg coda followed by an emerging coda after the Rayleigh arrival. The westerly section has lower transverse levels than the southwestern section. Coherent propagating waveforms can be seen propagating on the transverse component in the southwesterly direction. Peak amplitudes of the transverse component waves propagating to the southwest exceed 1/2 of the radial component peak amplitudes.



190 sec

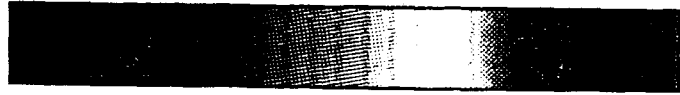
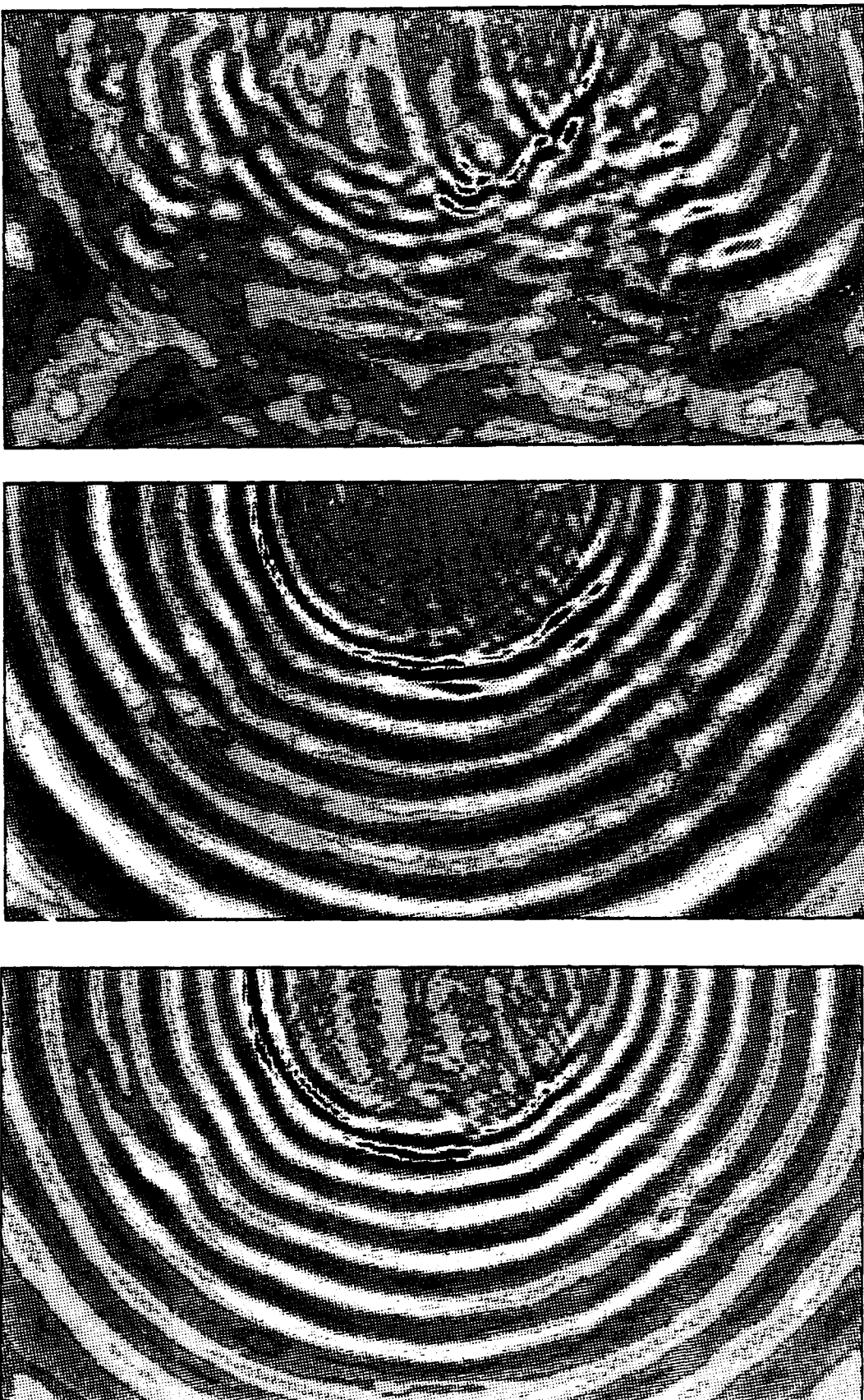


Figure 9a.

Snapshots (at 190 seconds) of the displacement field on the surface of the 3D finite difference grid. The vertical (Z) and radial (R) components of motion show the development of the asymmetrical Rayleigh wave propagation while the transverse (T) shows the developing Love wave coda.



290 sec



Figure 9b.

Snapshots (at 290 seconds) of the displacement field on the surface of the 3D finite difference grid. The vertical (Z) and radial (R) components of motion show the development of the asymmetrical Rayleigh wave propagation while the transverse (T) shows the Rayleigh to Love conversion that occurs along the edges of the sedimentary basins.



350 sec

Figure 9c.

Snapshots (at 350 seconds) of the displacement field on the surface of the 3D finite difference grid. The vertical (Z) and radial (R) components of motion show focusing by the low-velocity sedimentary basins. The transverse (T) shows Rayleigh to Love conversion along the edges of the sedimentary basins.

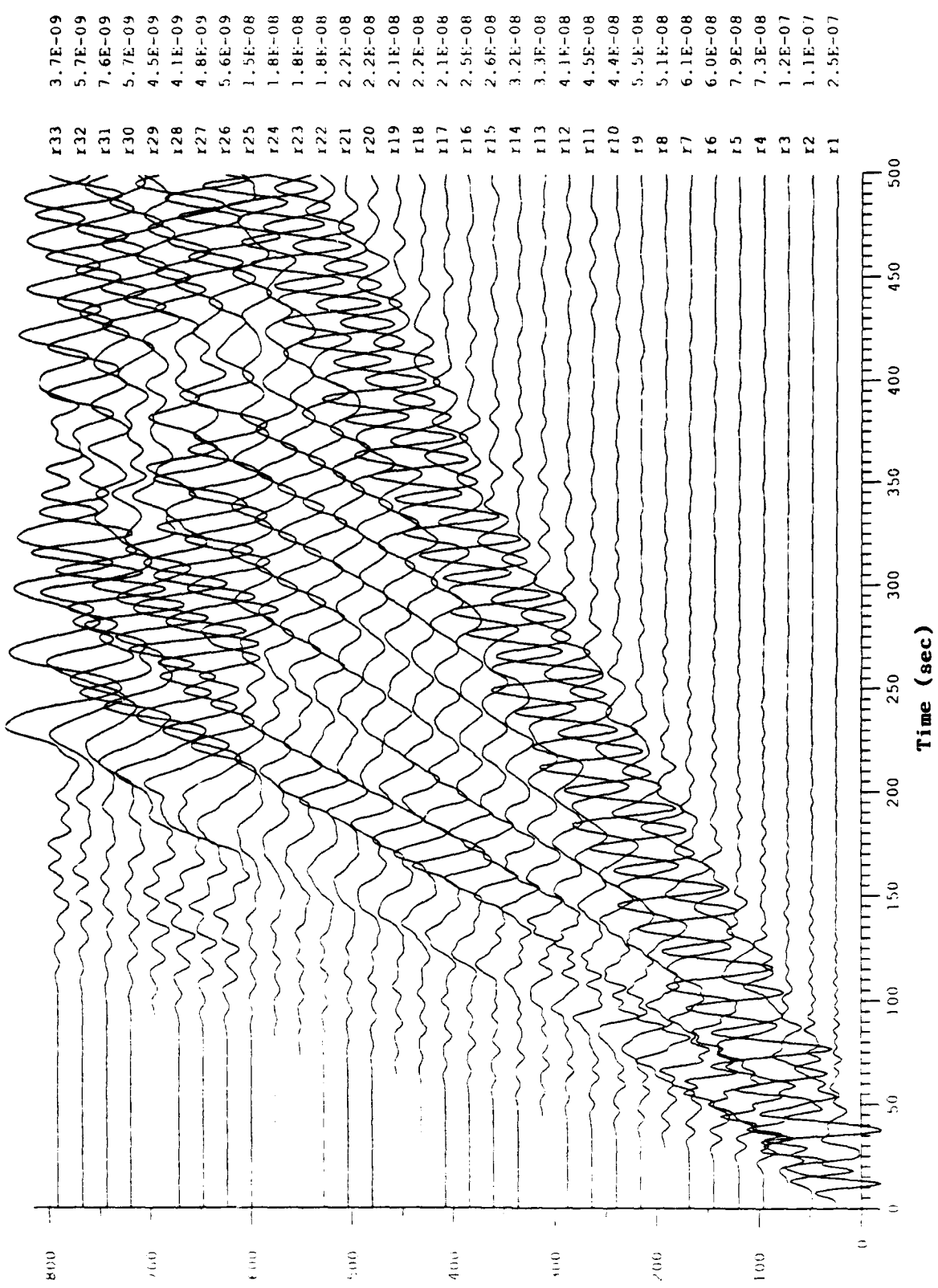


Figure 10a. Vertical displacement seismogram section to the west (270 degrees). Relative peak amplitude values are shown to the right of each trace.

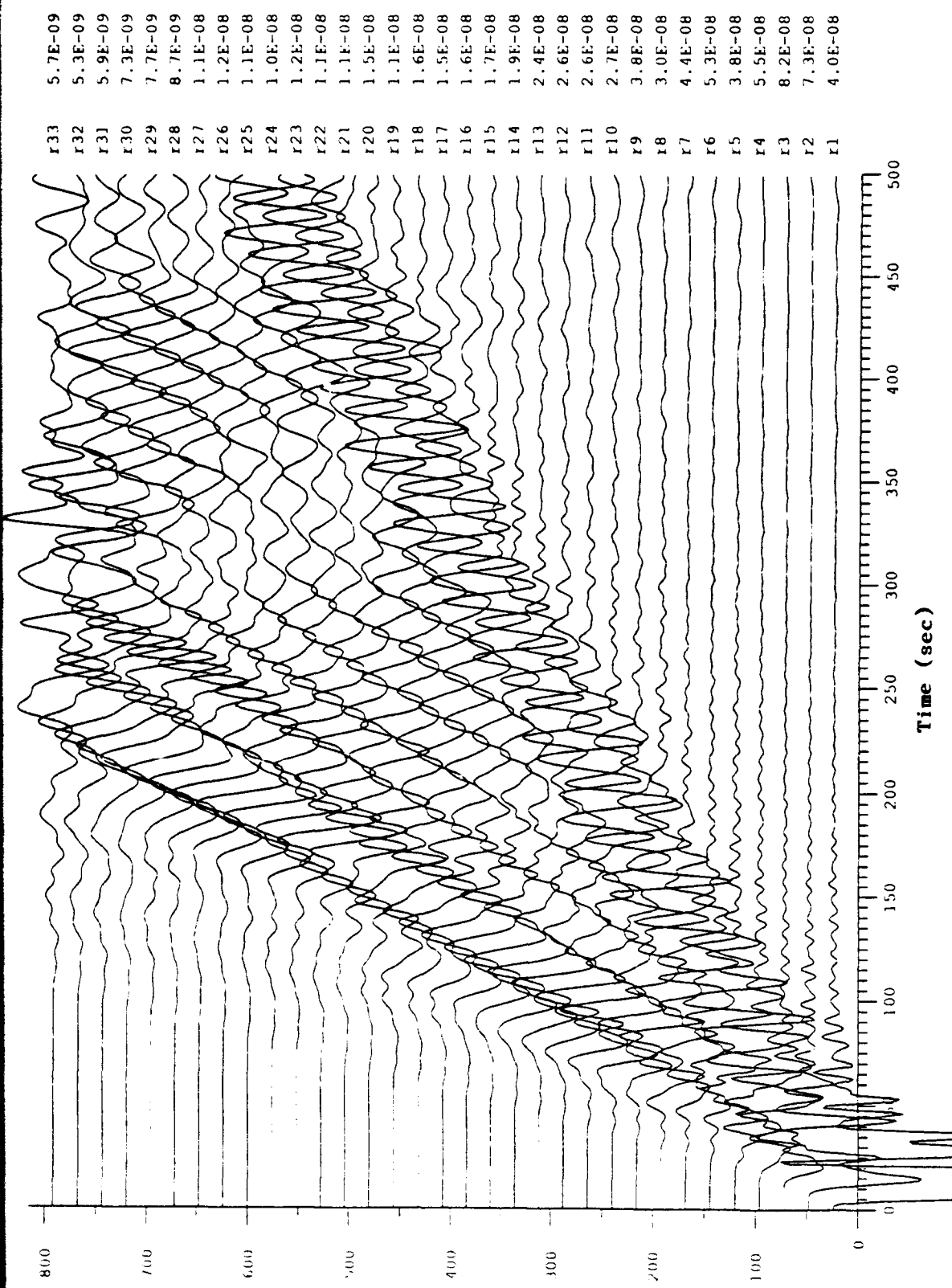


Figure 10b. Radial displacement seismogram section to the west (270 degrees). Relative peak amplitude values are shown to the right of each trace.

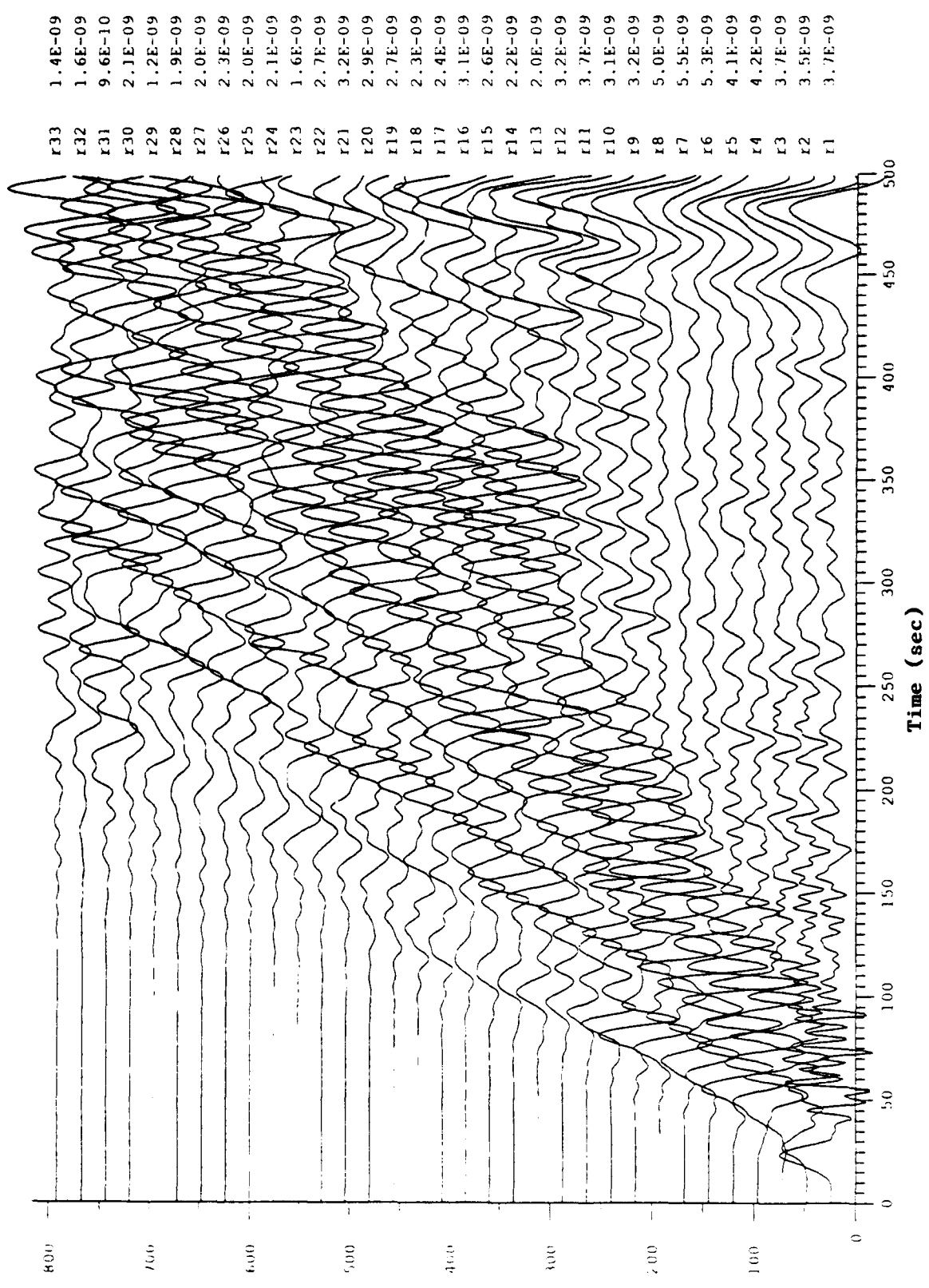


Figure 10c. Transverse displacement seismogram section to the west (270 degrees). Relative peak amplitude values are shown to the right of each trace.

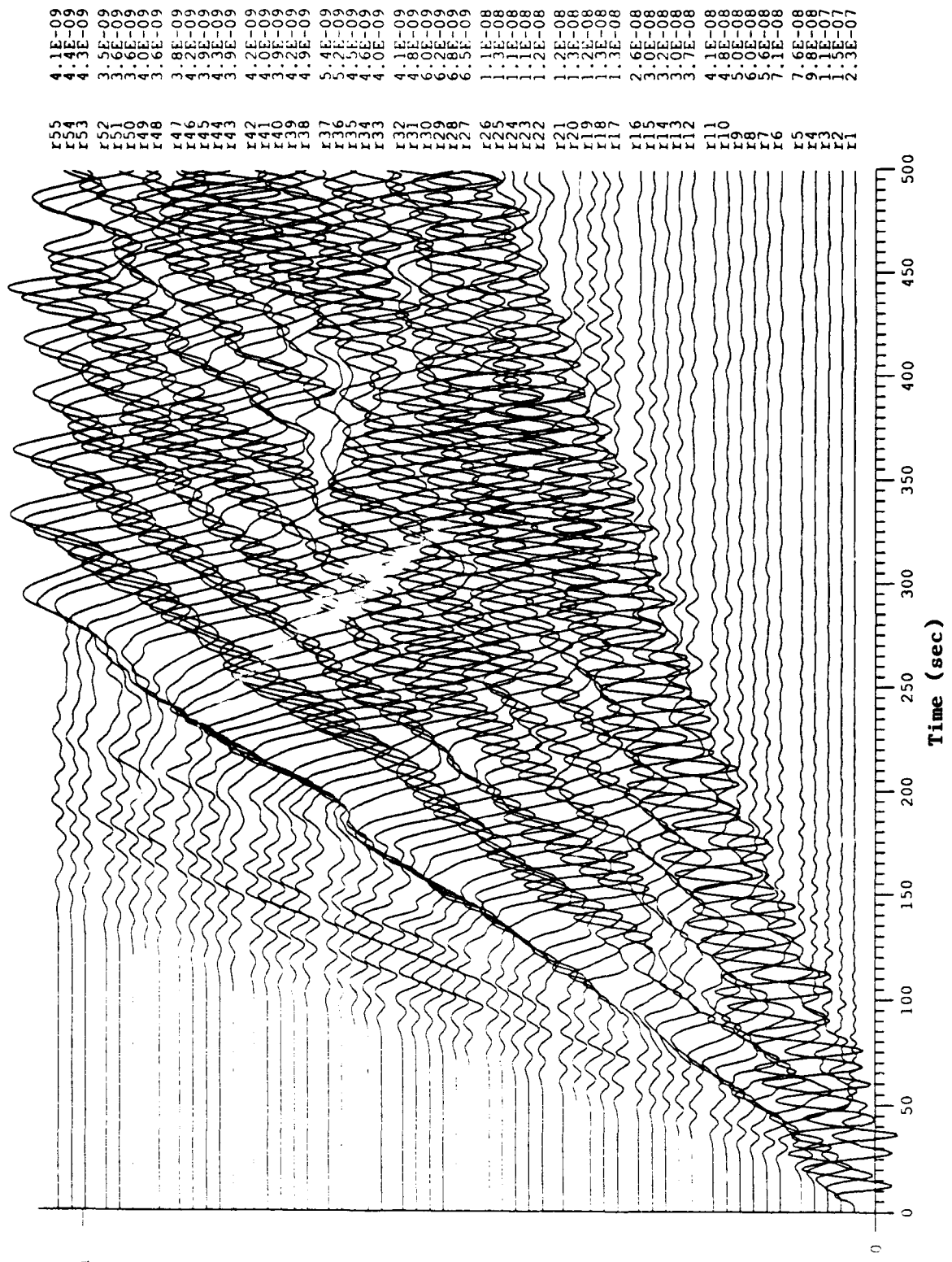


Figure 11a. Vertical displacement seismogram section to the southwest (220 degrees). Relative peak amplitude values are shown to the right of each trace.

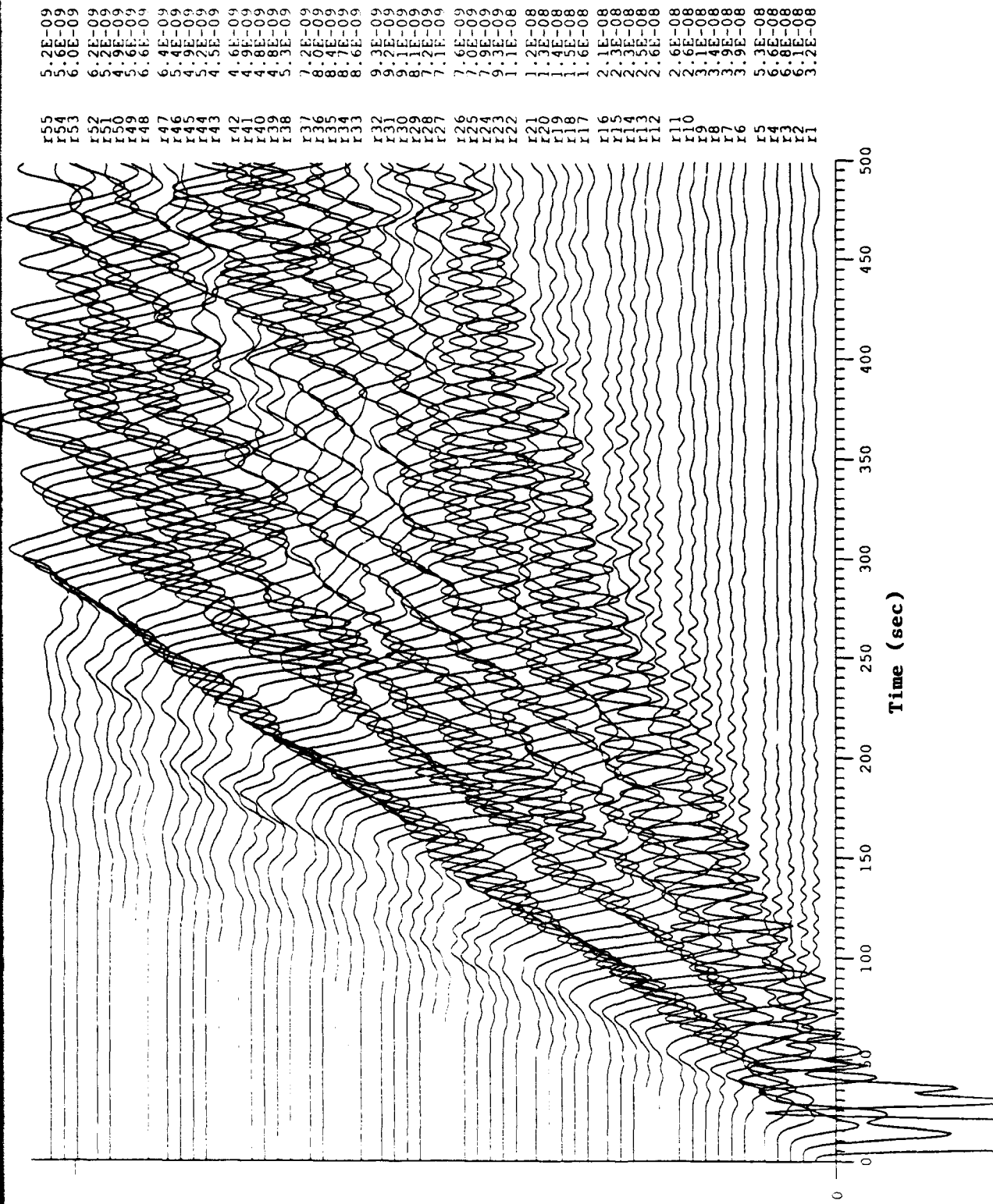


Figure 11b. Radial displacement seismogram section to the southwest (220 degrees). Relative peak amplitude values are shown to the right of each trace.

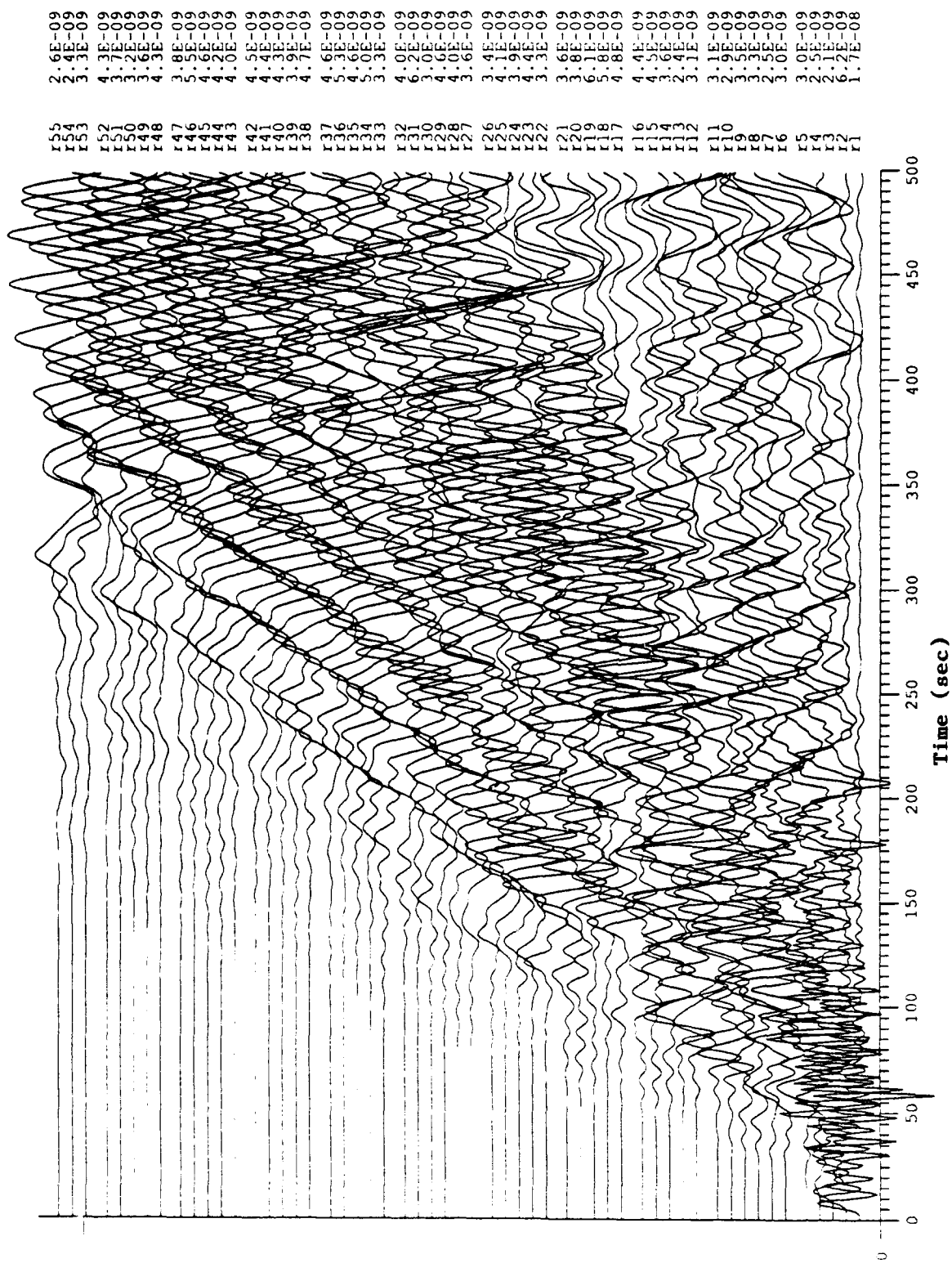


Figure 11c. Transverse displacement seismogram section to the southwest (220 degrees). Relative peak amplitude values are shown to the right of each trace.

In order to get a better picture of the frequency dependence of amplitudes in the grid, narrow band filters were applied to the vertical component seismograms and the peak amplitudes are contoured for 25, 30, 40, and 50 second periods in Figures 12a,b,c,d. The amplitudes have been multiplied by \sqrt{R} in order to make a partial correction for geometrical spreading. Note that asymmetries are present at all periods. The amplitude contours of the short period waves (25 and 30 seconds) outline some of the deep sedimentary basins. The longer period amplitude contours clearly show how the amplitudes are larger to the west than to the north or south.

The same processing was repeated for the radial and transverse components of motion. The peak amplitude contours at 25 and 40 second periods are shown in Figures 13a,b and Figures 14a,b. The transverse motion is minimum to the west, north, and south with several ridges of high amplitude extending to the northwest and southwest. These high amplitude ridges of radial and transverse components at 25 second period correlate with the radial extension of the edges and corners of sedimentary basins. The zones of Rayleigh-to-Love conversion at 25 and 40 second periods are best seen in Figures 15a,b where the T/R ratio is contoured.

In addition to the peak amplitudes at selected periods, the processing of the seismograms can yield the phase and group delays at each location on the surface of the grid. Group delays are shown for 25, 30, 40, and 50 second periods in Figures 16a,b,c,d. Wave energy travels normal to group delay contours, and this analysis serves to show that the direction of propagation is complicated to the northwest and southwest. Even the long period (50 second) group delay contours show the effects of lateral refraction. At the shortest period (25 seconds) large perturbations in the wavefront can be seen along the southern boundary of the Barents Shelf. The slow structures to the west retard the waves while the faster structures to the south-southwest allow a faster route for the wave energy. Multipathing at 25 second periods becomes evident where contours close in on themselves to the southwest and northwest.

Similarly, phase delay contours can be constructed across the grid surface and the average phase velocity from source to receiver can be contoured. Figure 17a,b shows these contours of phase delay and inferred

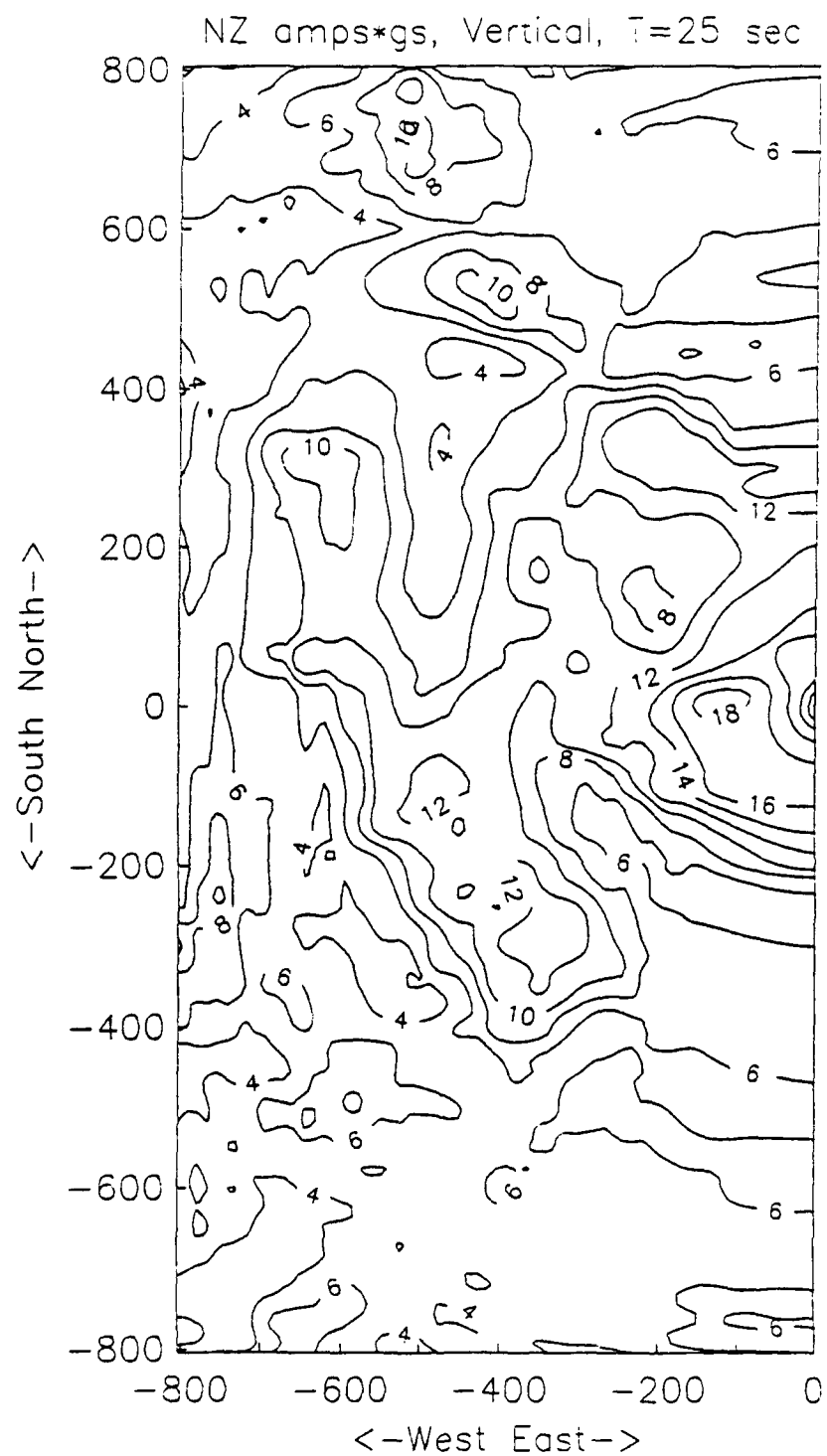


Figure 12a. Contours of 25 second period peak vertical Rayleigh wave amplitudes with $1/\sqrt{R}$ geometrical spreading correction on the surface of the 3D grid. Note the asymmetries associated with the sedimentary basins.

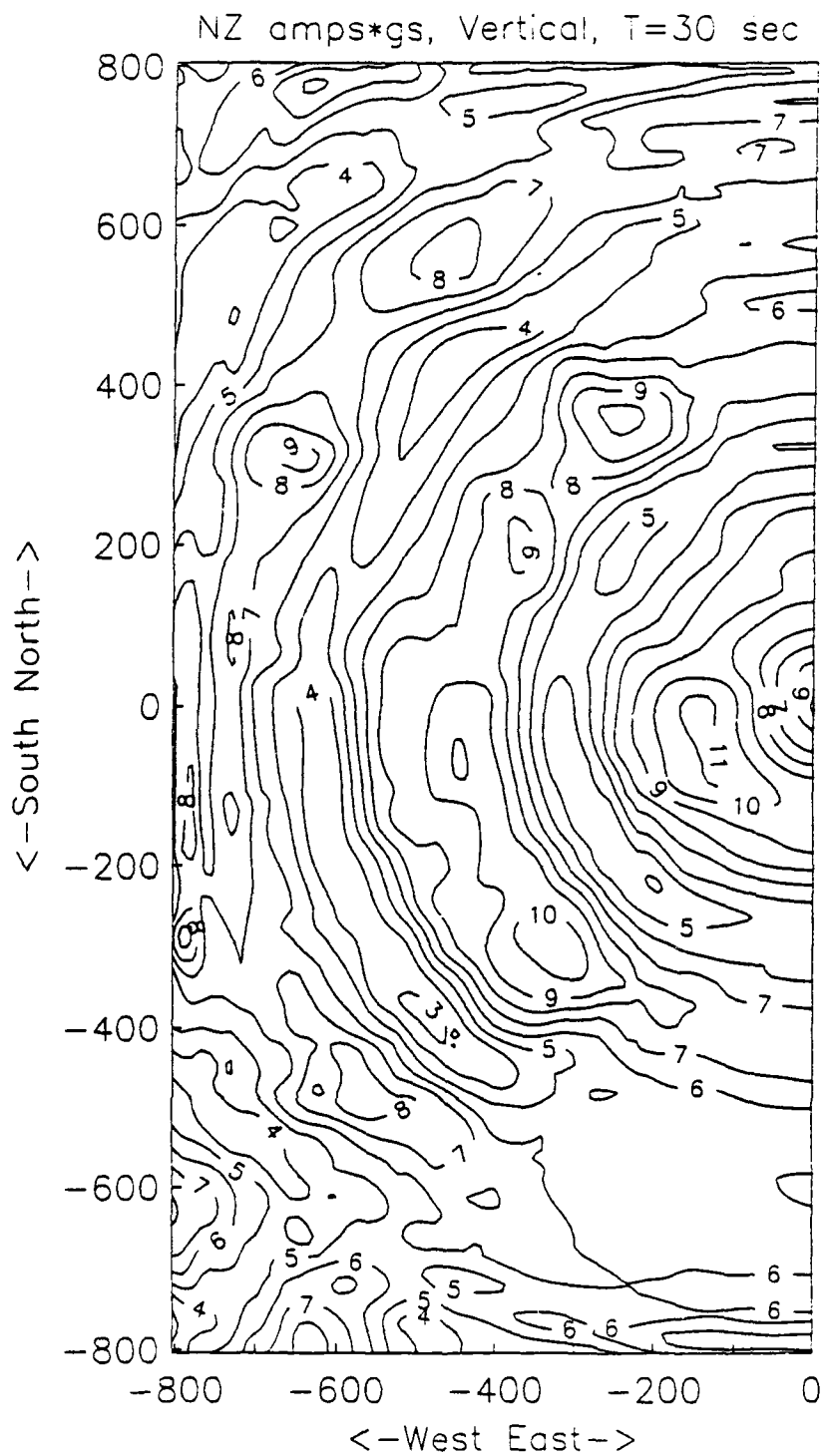


Figure 12b. Contours of 30 second period peak vertical Rayleigh wave amplitude on the surface of the 3D grid. Note the asymmetries associated with the sedimentary basins.

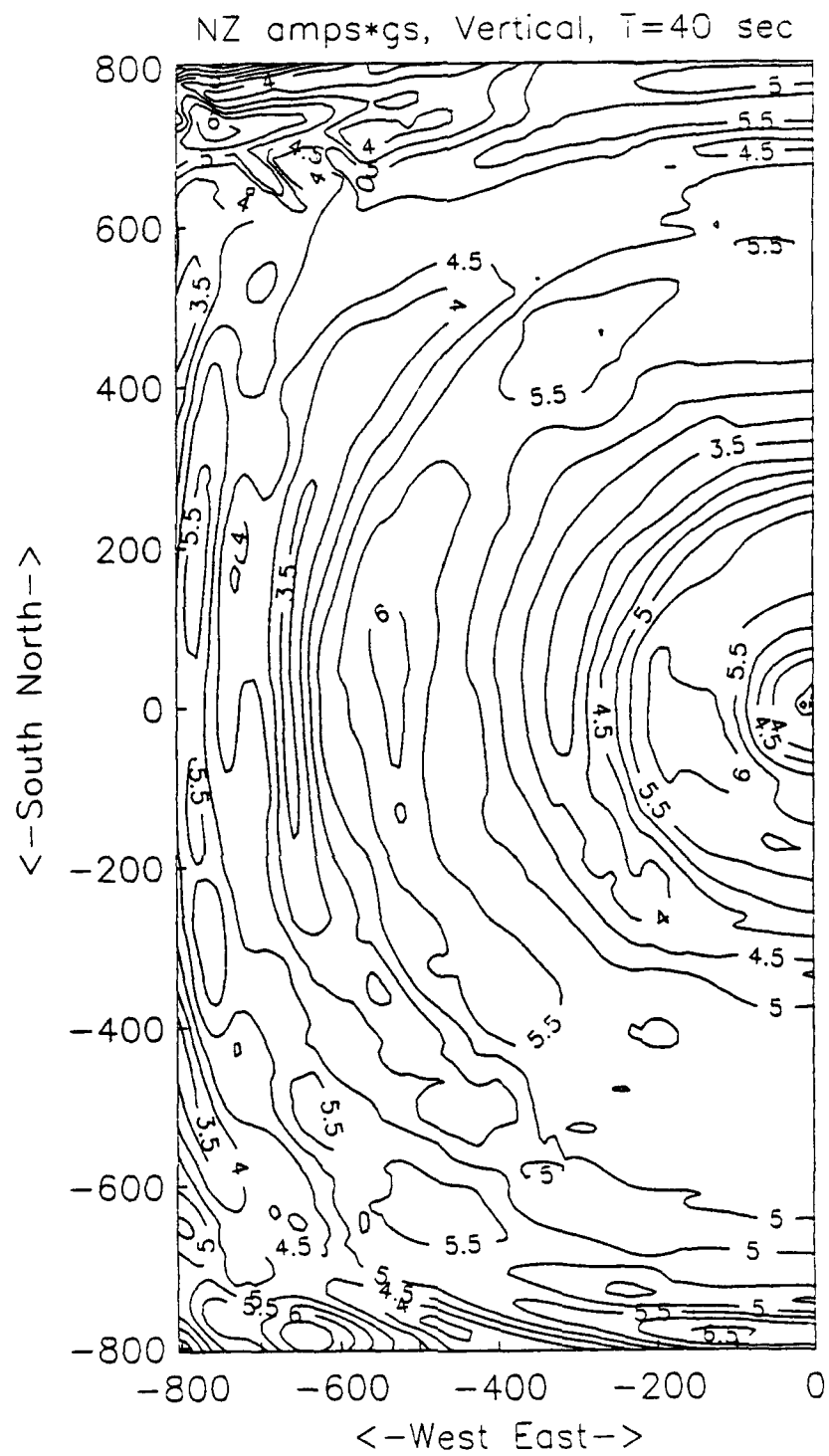


Figure 12c. Contours of 40 second period peak vertical Rayleigh wave amplitude on the surface of the 3D grid. Note the asymmetries associated with the sedimentary basins.

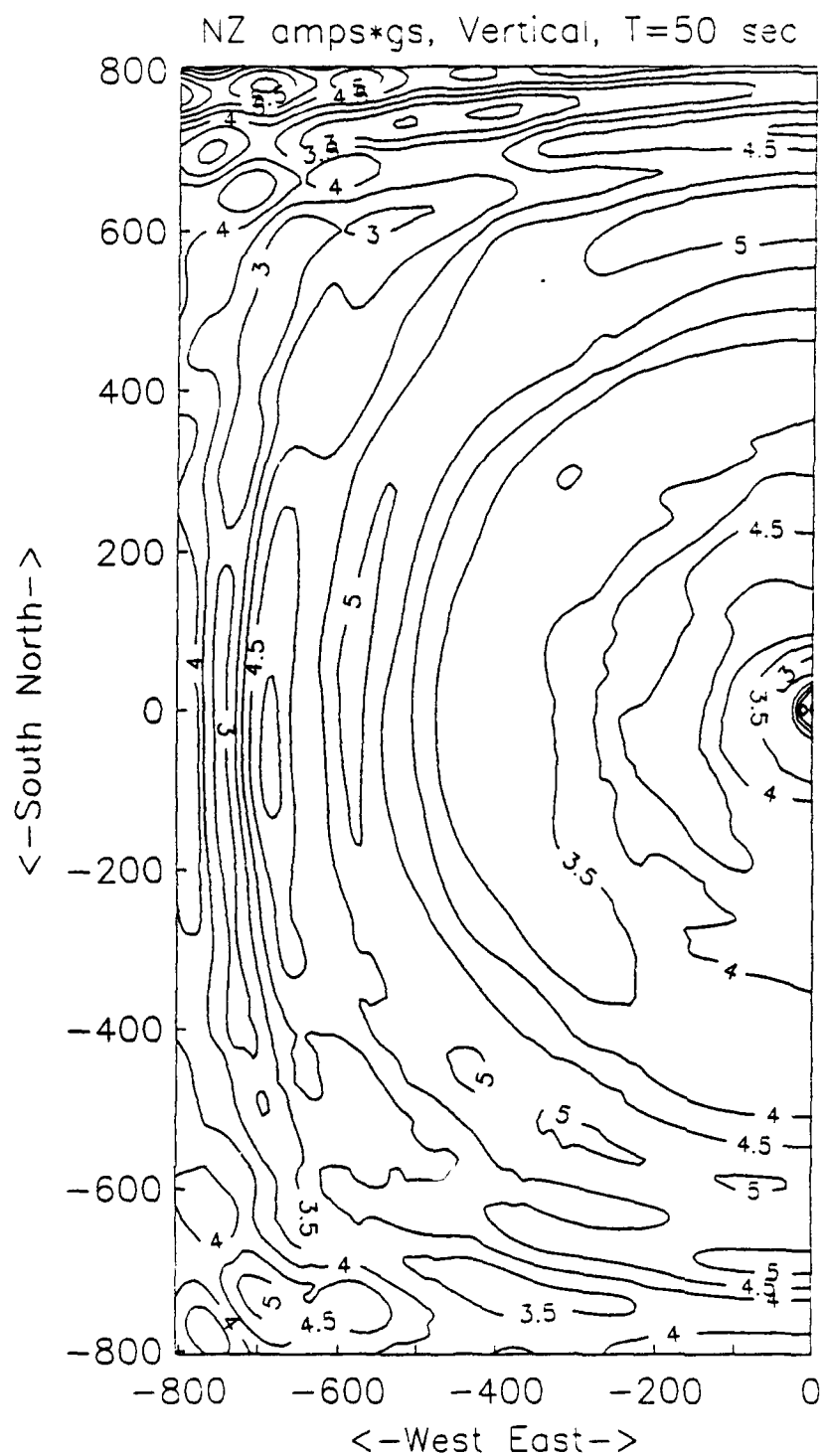


Figure 12d. Contours of 50 second period peak vertical Rayleigh wave amplitude on the surface of the 3D grid. Note the focusing of waves propagating to the west.

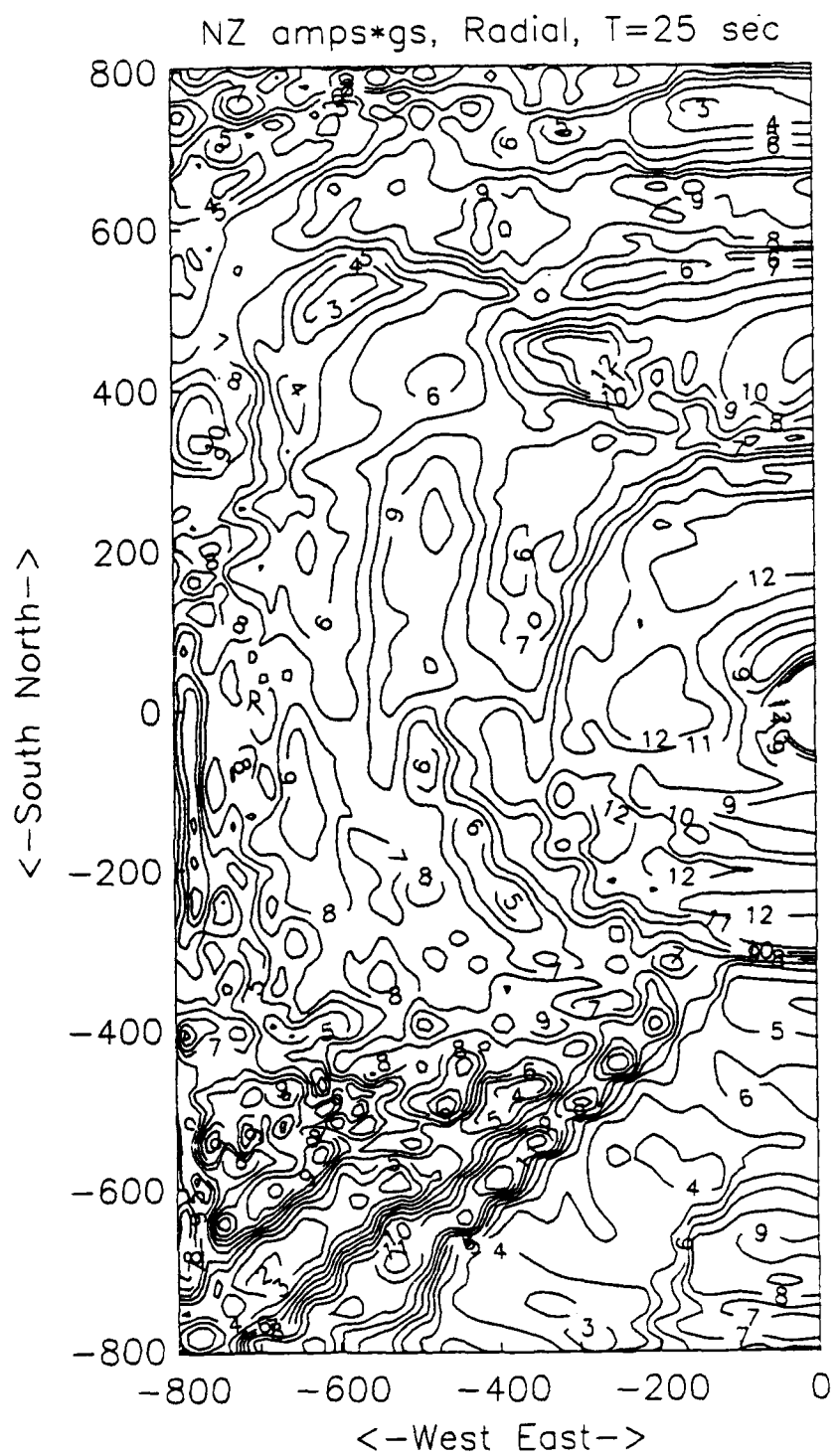


Figure 13a. Contours of 25 second period peak radial amplitudes with $1/\sqrt{R}$ geometrical spreading correction on the surface of the 3D grid.

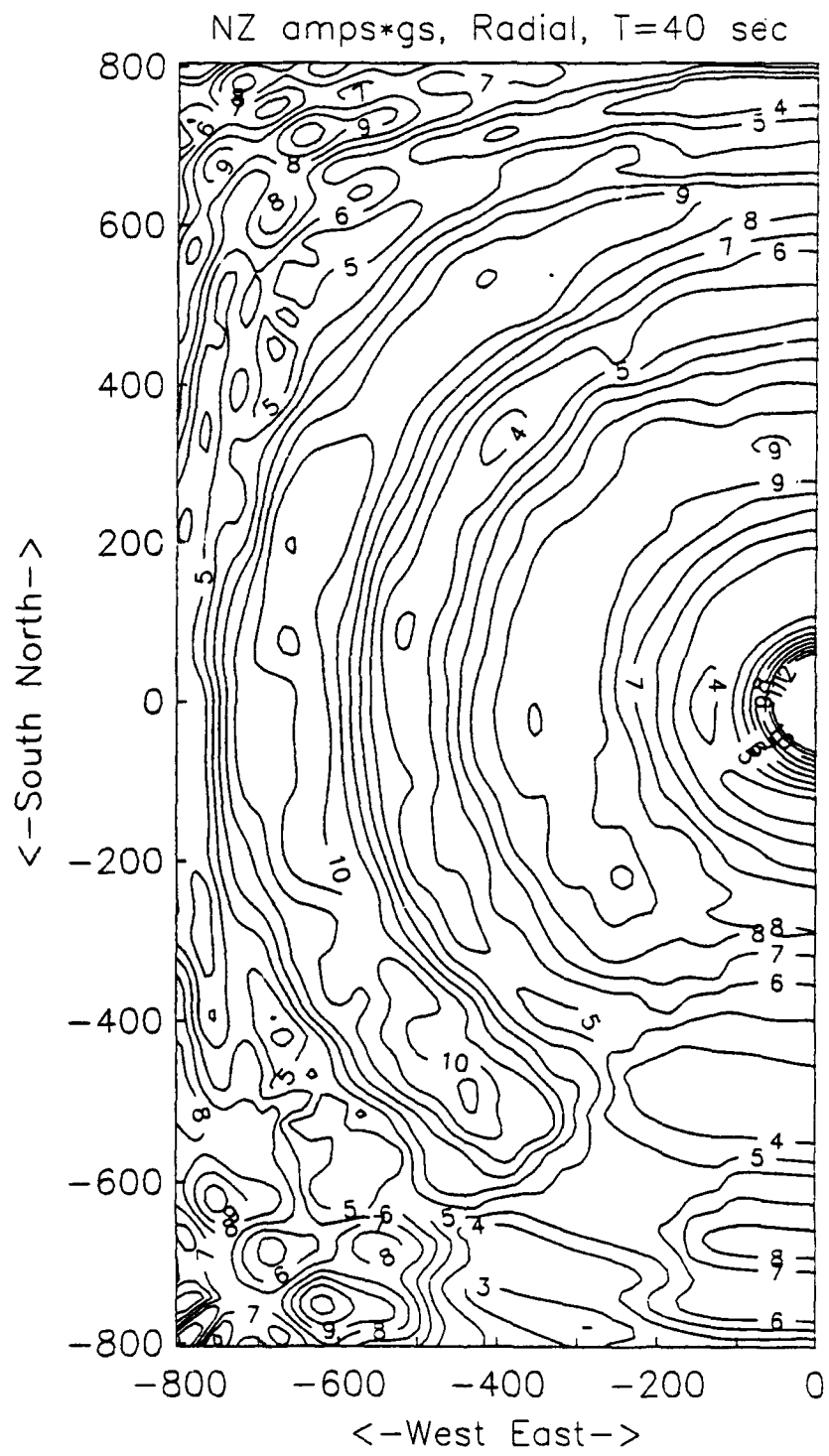


Figure 13b. Contours of 40 second period peak radial amplitudes with $1/\sqrt{R}$ geometrical spreading correction on the surface of the 3D grid.

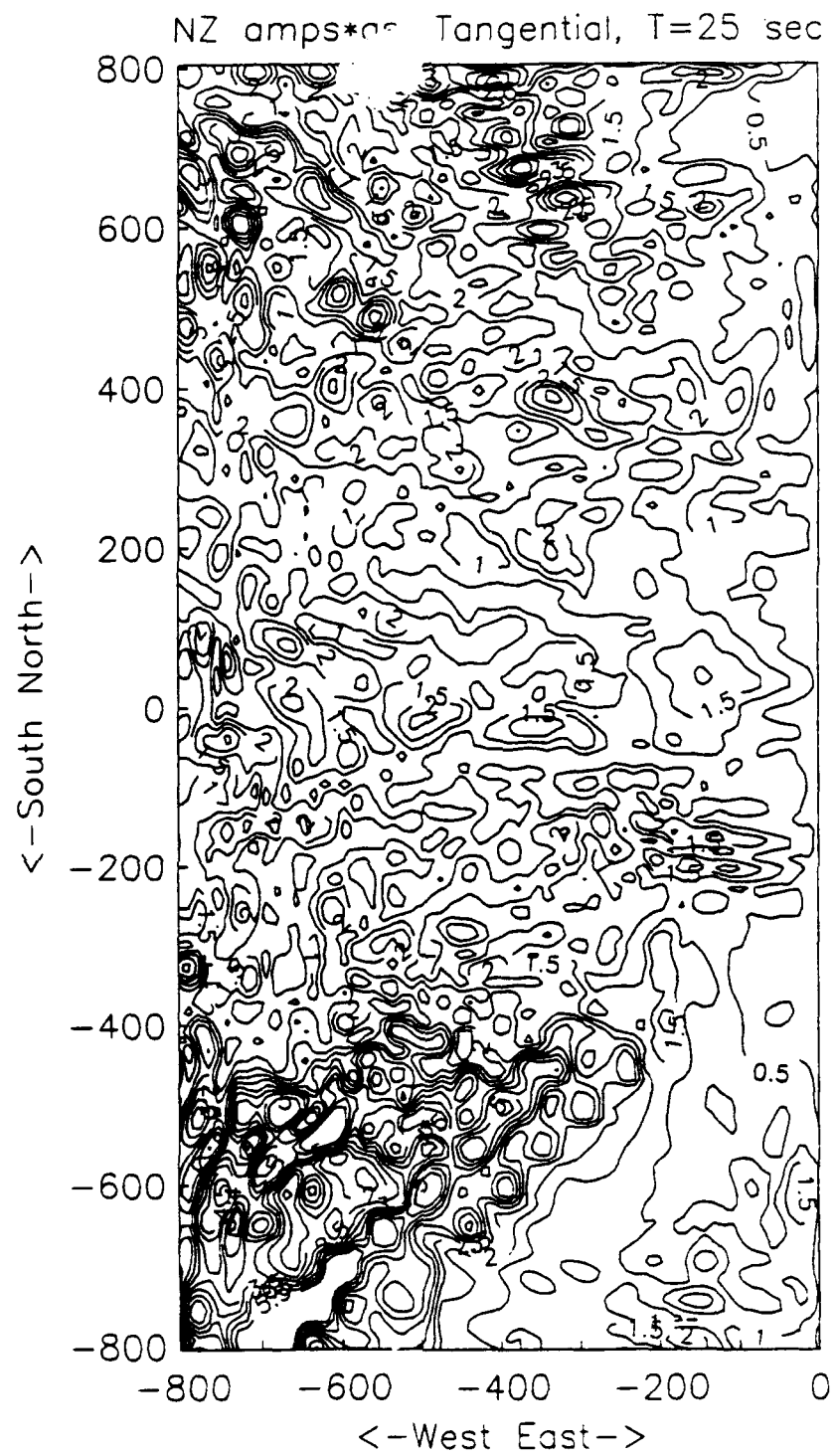


Figure 14a. Contours of 25 second period peak transverse amplitudes with $1/\sqrt{R}$ geometrical spreading correction on the surface of the 3D grid.

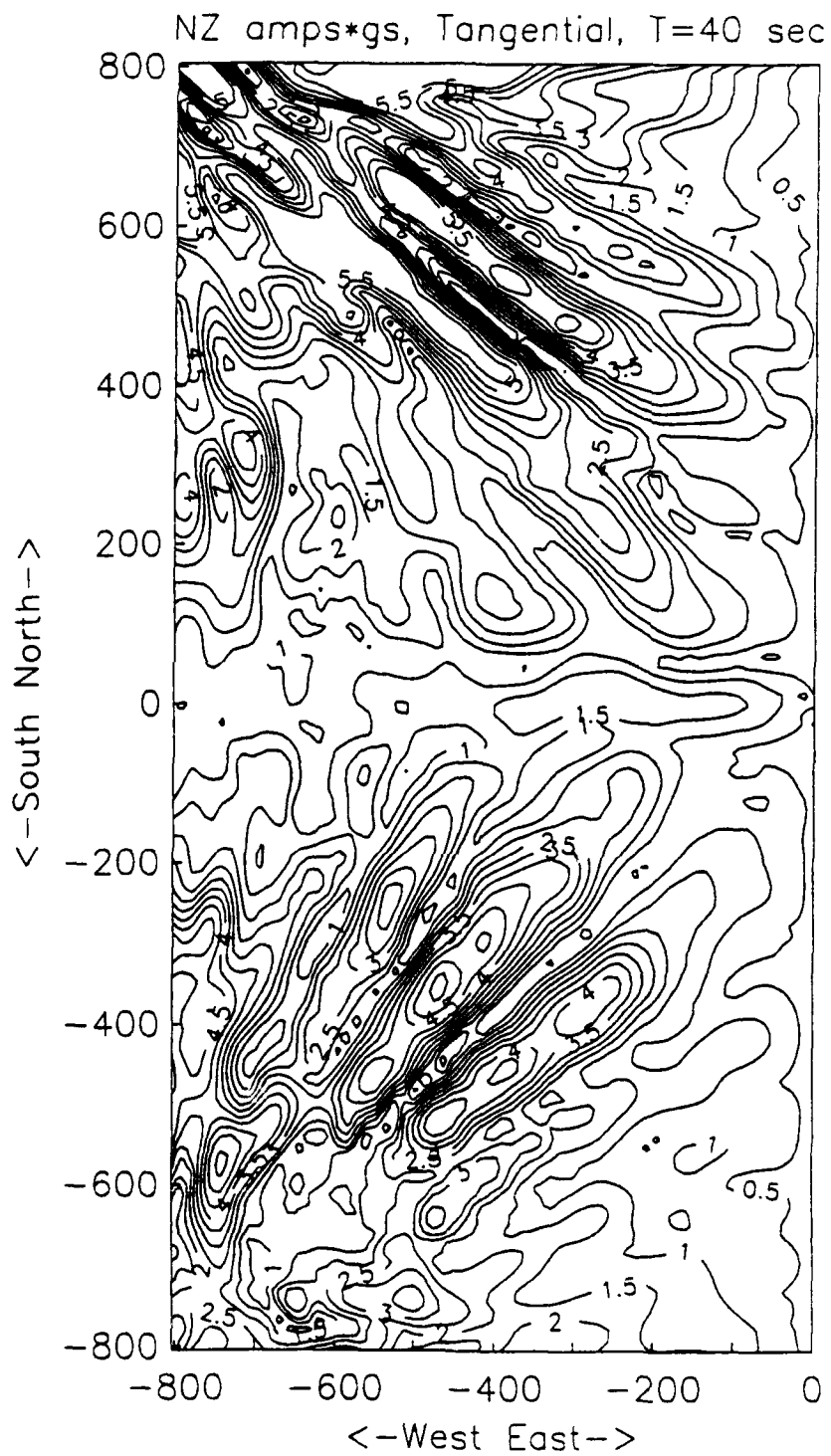


Figure 14b. Contours of 40 second period peak transverse amplitudes with $1/\sqrt{R}$ geometrical spreading correction on the surface of the 3D grid.

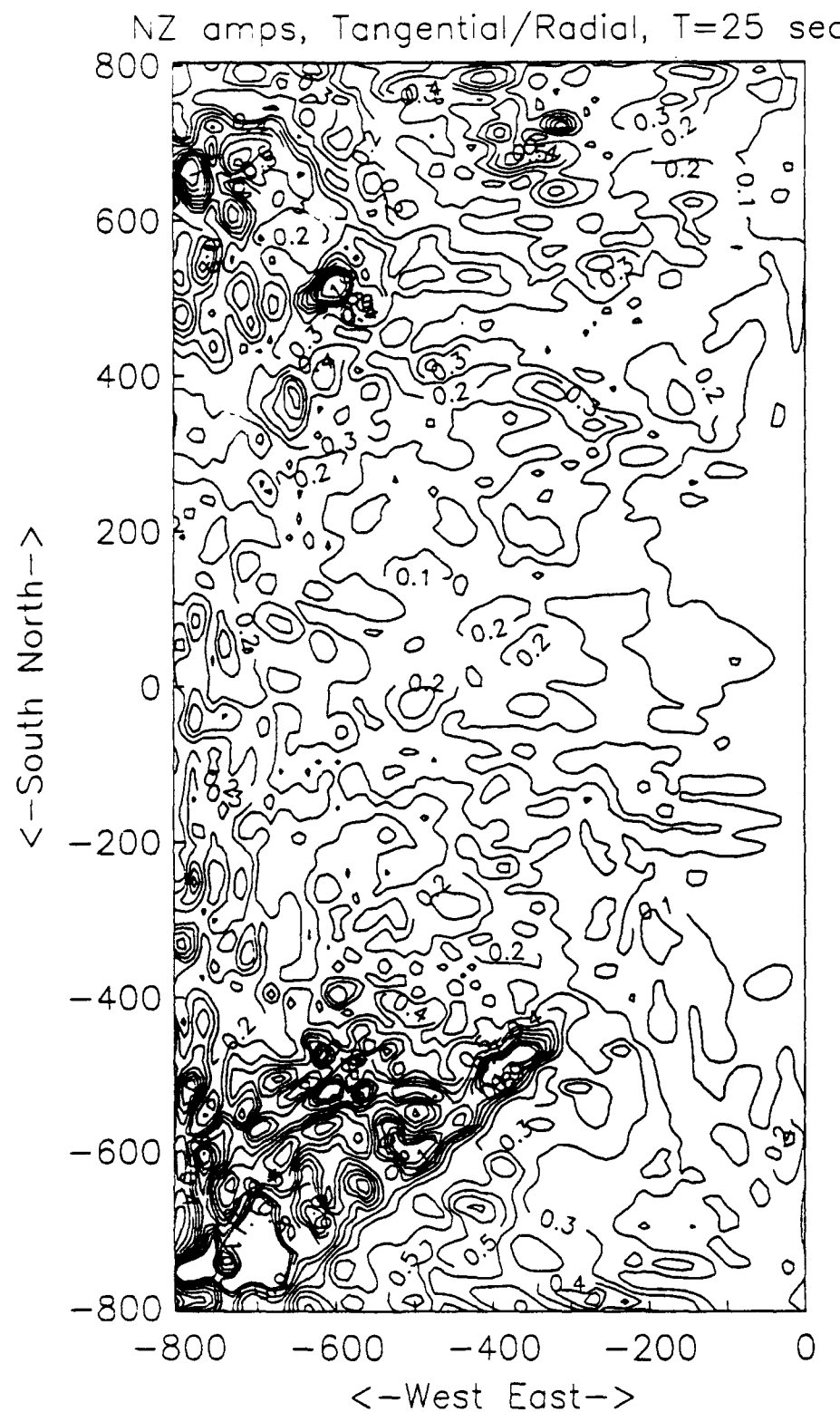


Figure 15a. Contours of the ratio of Transverse/Radial 25 second period motion on the surface of the 3D grid.

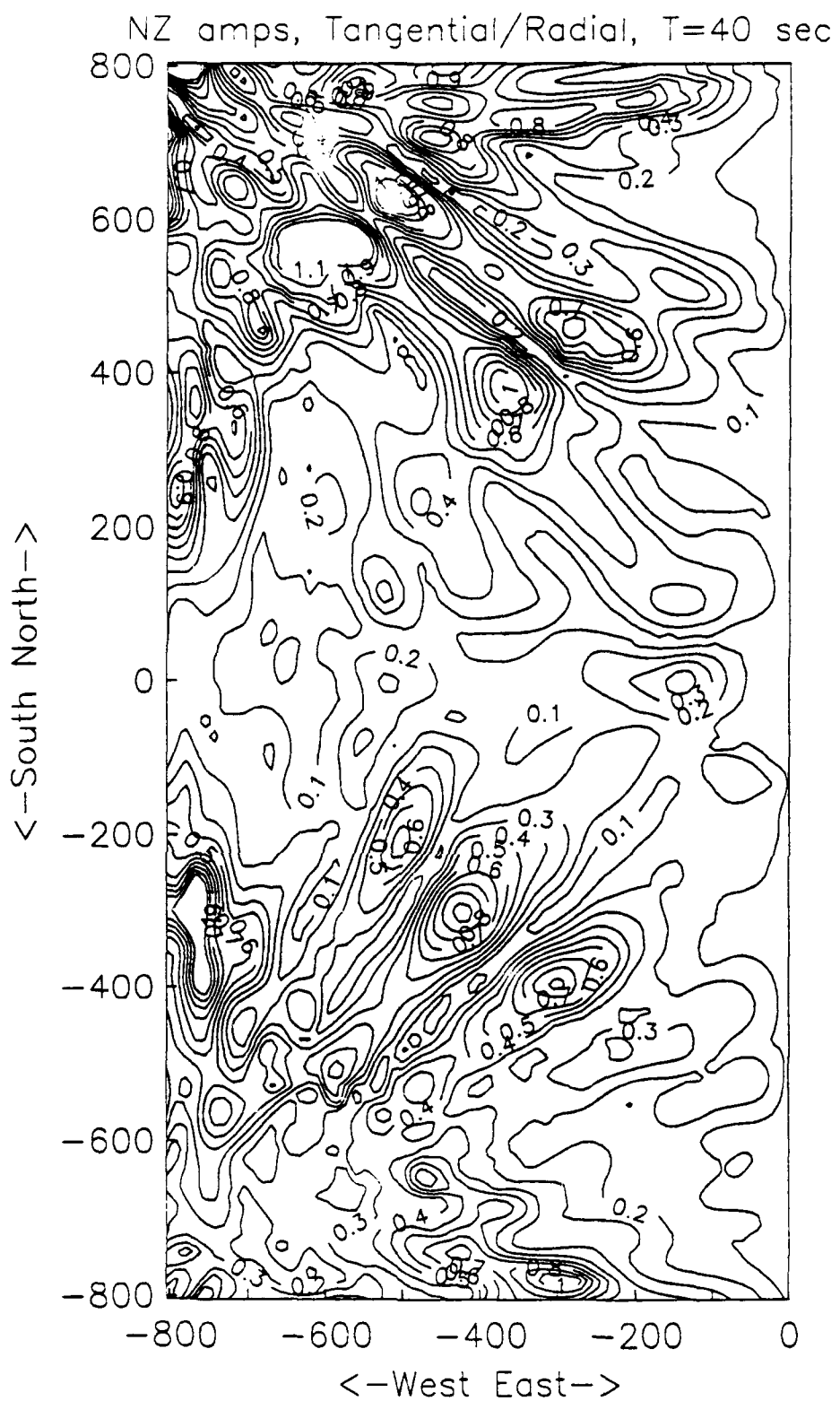


Figure 15b. Contours of the ratio of Transverse/Radial 40 second period motion on the surface of the 3D grid.

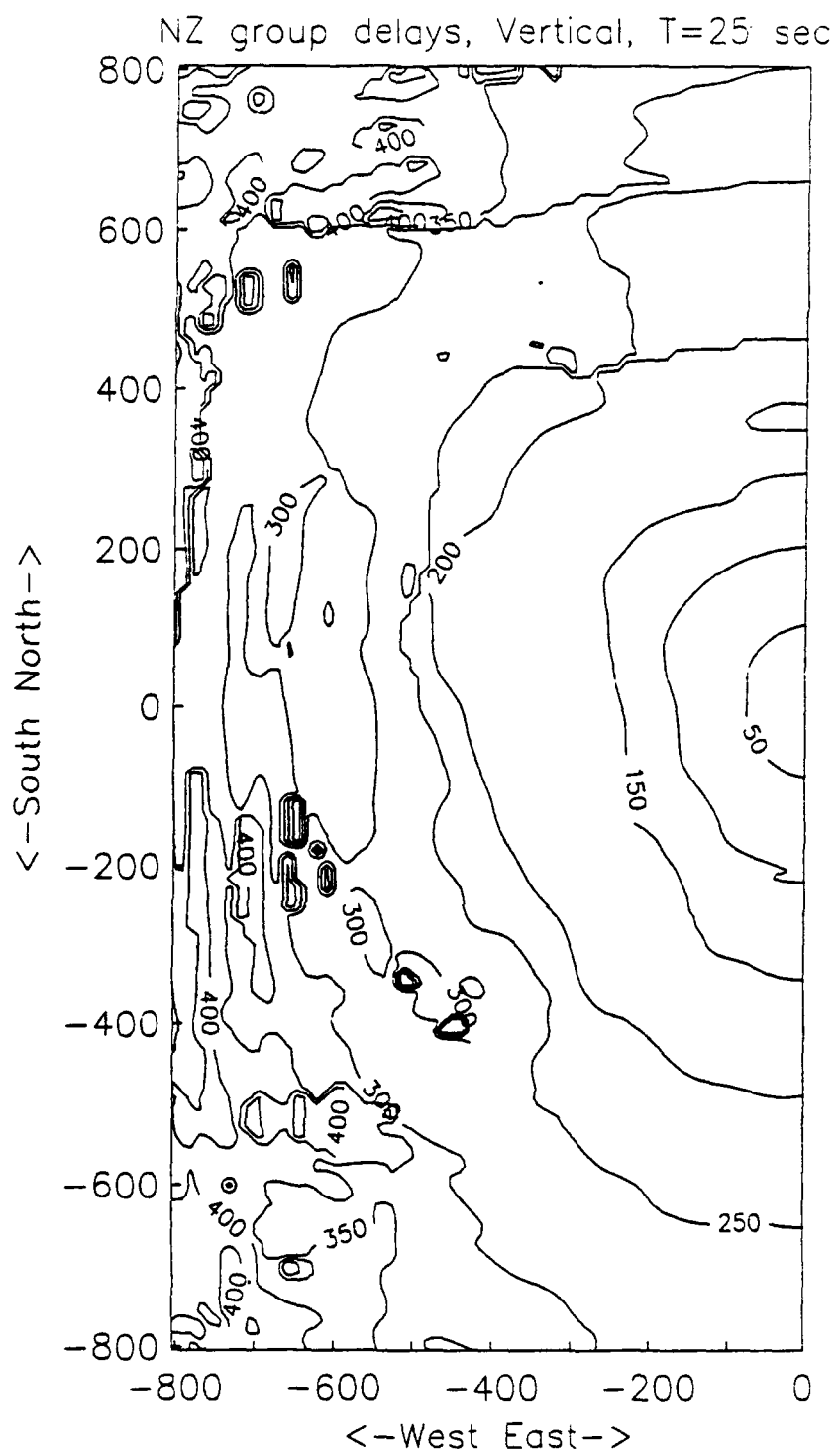


Figure 16a. Group delay contours for 25 second period vertical Rayleigh waves on the surface of the 3D grid. Contours show wave energy refracting around the Barents Shelf sedimentary basins to the southwest of the source. Complexity of the contours at distances greater than 500 km from the source suggest multipathing at 25 second periods.

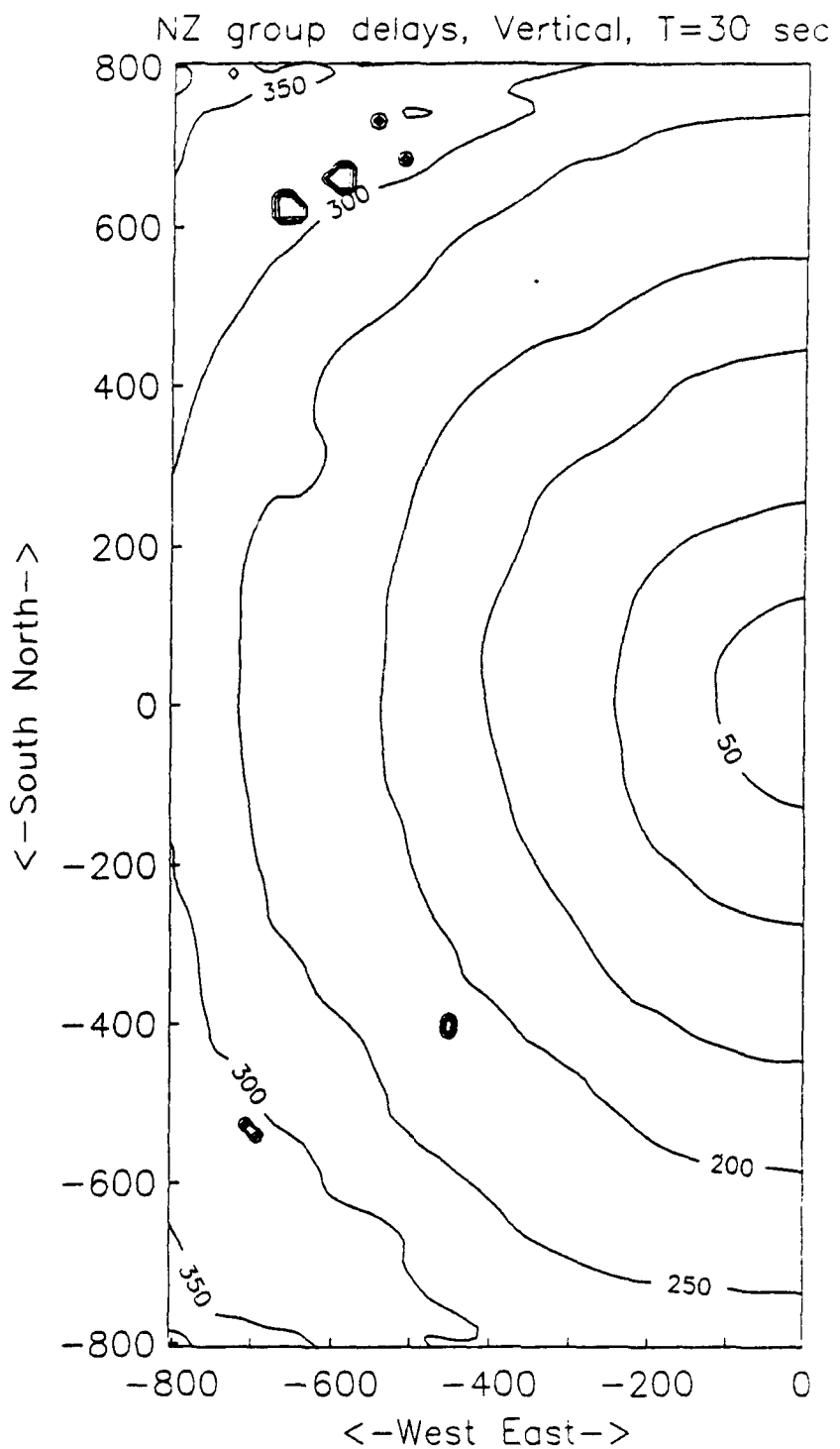


Figure 16b. Group delay contours for 30 second period vertical Rayleigh waves on the surface of the 3D grid. Compared to 25 second period waves the 30 second period waves do not show the complexity of group delay contours.

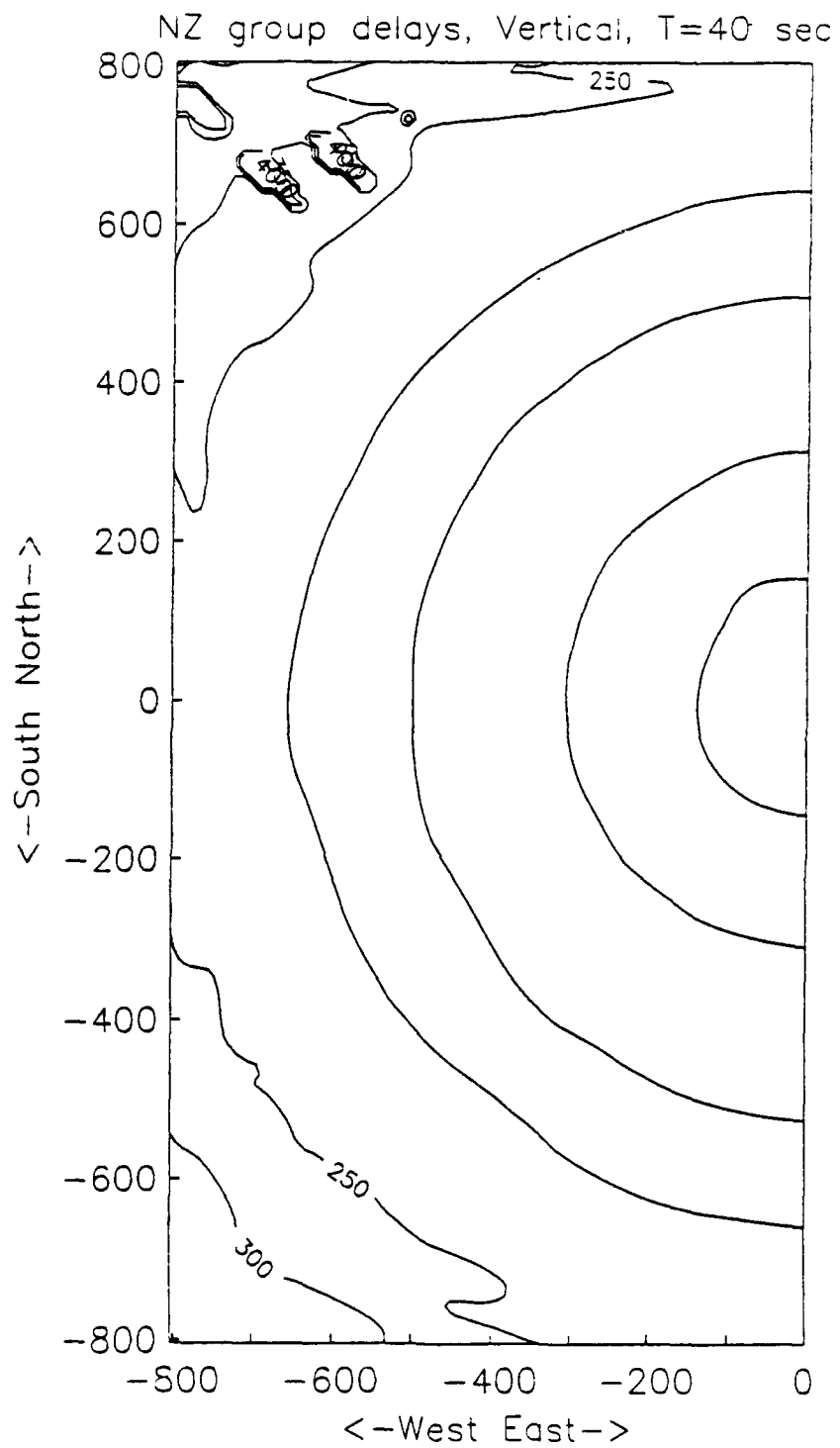


Figure 16c. Group delay contours for 40 second period vertical Rayleigh waves on the surface of the 3D grid. Deviations from circles are clearly seen as the 40 second waves are delayed by the low-velocity structures.

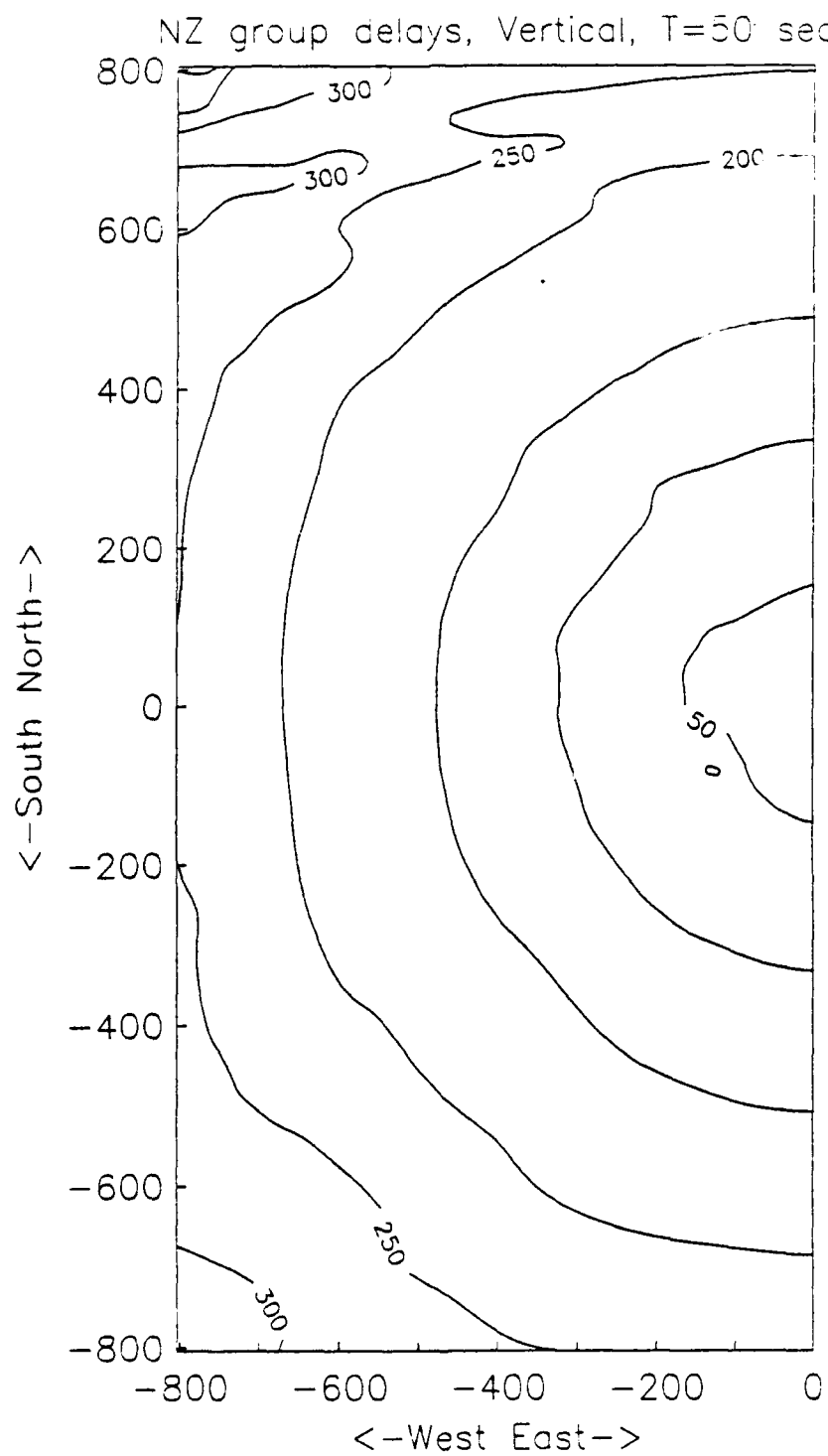


Figure 16d. Group delay contours for 50 second period vertical Rayleigh waves on the surface of the 3D grid. Deviations from circles are clearly seen as the 50 second waves are delayed by the low-velocity structures.

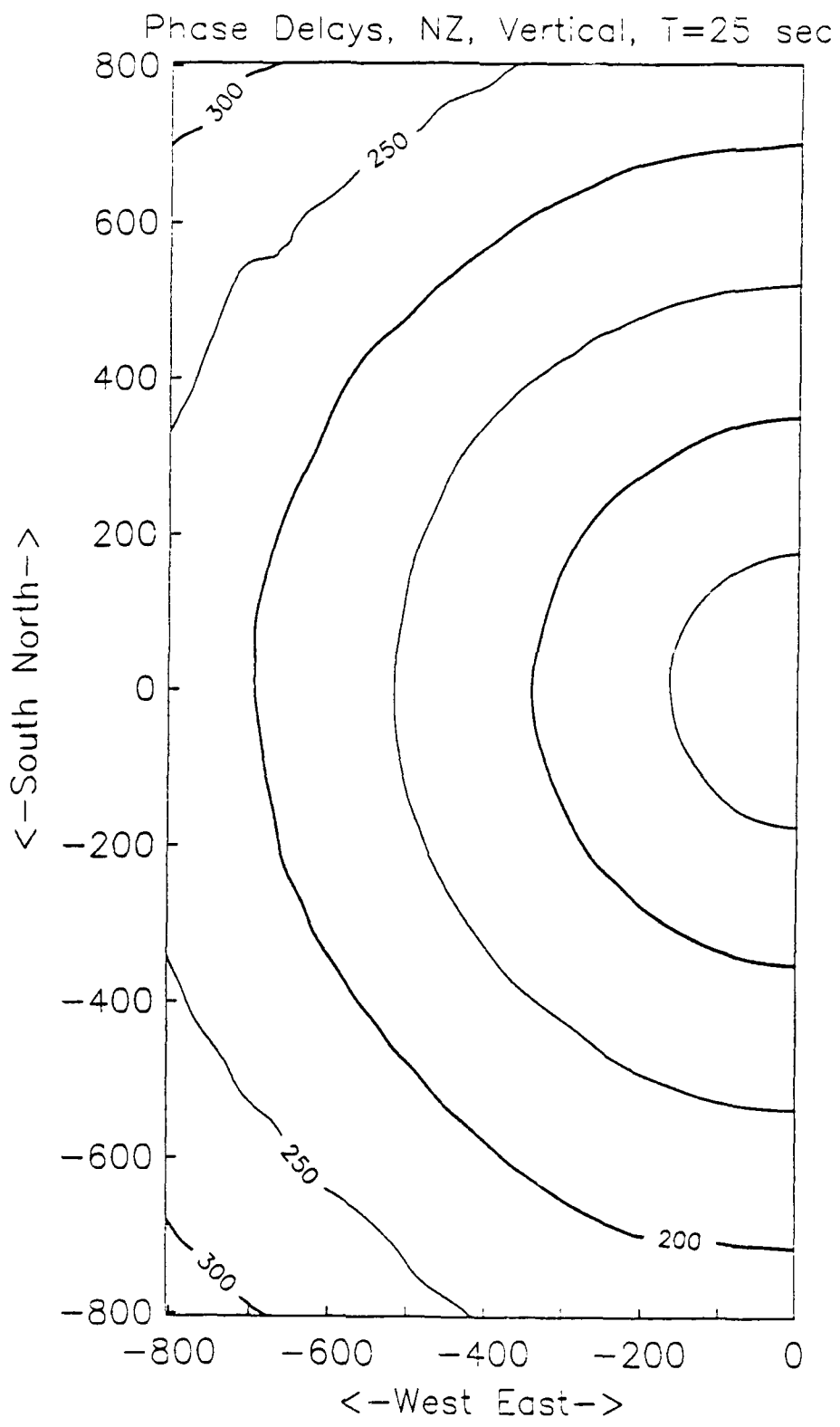


Figure 17a. Phase delay contours for 25 second period vertical Rayleigh waves on the surface of the 3D grid.

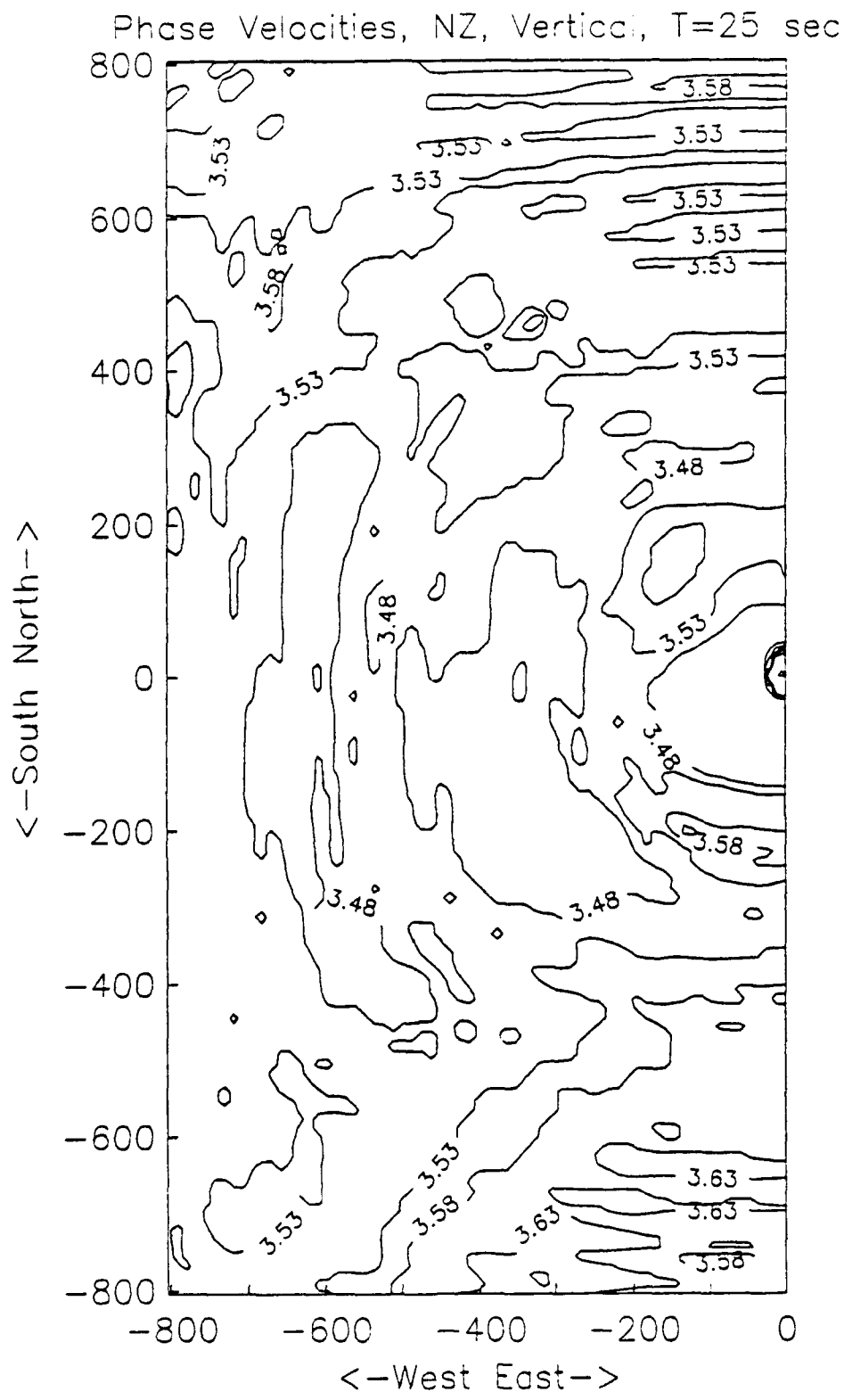


Figure 17b. Inferred phase velocity contours for 25 second period vertical Rayleigh waves on the surface of the 3D grid. Phase delay has been converted to phase velocity. The southeastern edge of the sedimentary basin to the southwest of the source can be seen as a gradient in the phase velocities.

phase velocity for 25 second period vertical component Rayleigh waves. The phase velocity contours are lowest in the basins with gradients serving to highlight the edges of the low-to-high velocity structural contacts.

Broadband (0.04 to 0.05 Hz) frequency-wavenumber (fk) processing for two 25 station arrays on the surface of the grid are displayed in Figure 18a, and b. The array in the southwest corner of the grid (Figure 18a) shows Rayleigh wave energy (vertical and radial components) arriving on azimuth while the transverse component motion arrives nearly 13 degrees off azimuth. The second array (Figure 18b) was placed to the south-southwest of the source and records vertical and radial motion only 7 degrees off azimuth while the transverse motion arrives 12 degrees off azimuth. Both arrays are recording the Rayleigh-to-Love conversions from the sedimentary basins southwest of the source.

To summarize, we see focusing/defocusing of surface waves with periods ranging from 25 to 50 seconds. Refraction and multipathing is greatest for the shortest wave lengths. Rayleigh-to-Love conversion is occurring where Rayleigh waves travel obliquely along boundaries between high and low velocity regions. Transverse motion for 40 and 25 second periods can locally exceed radial motion but regions of Rayleigh-to-Love conversion more typically exhibit T/R ratios between 1/4 to 1/2.

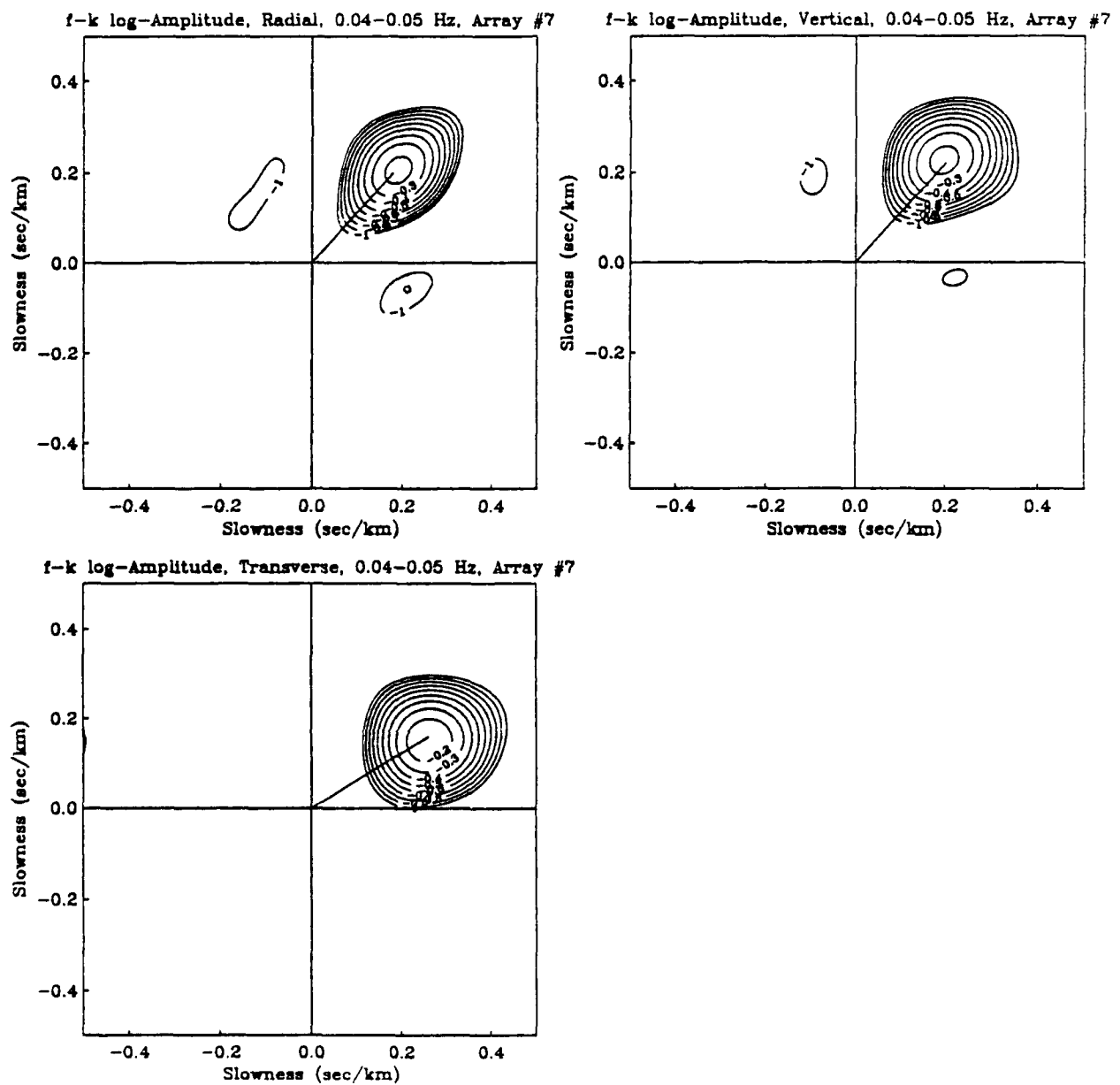


Figure 18a. Broadband (0.04 - 0.05 Hz) frequency-wavenumber (f-k) analysis of radial (upper left), vertical (upper right), and transverse (lower left) component motion from a 25 station array in the southwest corner of the grid. The source is at an azimuth of 45 degrees from the array. Radial and vertical energy is arriving from an azimuth of 42 degrees, transverse energy is arriving from an azimuth of 58 degrees.

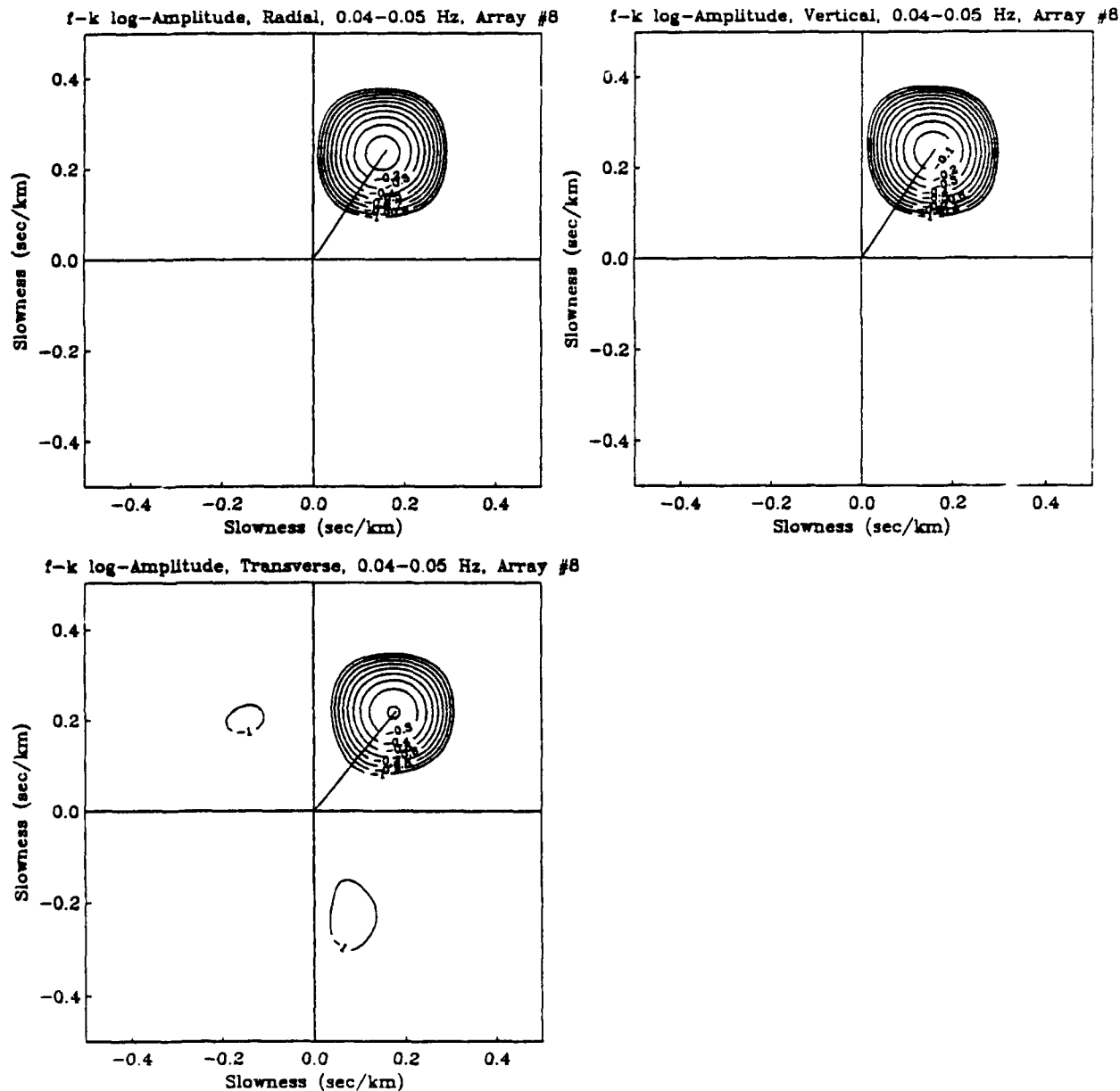


Figure 18b. Broadband (0.04 - 0.05 Hz) frequency-wavenumber (f-k) analysis of radial (upper left), vertical (upper right), and transverse (lower left) component motion from a 25 station array. The source is at an azimuth of 27 degrees from the array. Radial and vertical energy is arriving from an azimuth of 34 degrees, transverse energy is arriving from an azimuth of 39 degrees.

7. TELESEISMIC LR AMPLITUDES

In order to propagate the Rayleigh waves out of the finite difference grid to teleseismic distances we need to make some simplifying assumptions about the propagation outside the finite difference grid. In order to do this, we have applied the Fresnel-Kirchoff integral method as described in McLaughlin, *et al.* (1991) to predict the effects of near-source propagation (within 800 km) upon the amplitudes of teleseismic long-period Rayleigh waves. The vertical component Rayleigh waves observed on the surface of the 3D finite difference grid are propagated to teleseismic distance (5000 km) taking into account far-field diffraction effects. The far-field seismogram in the frequency domain, $S(f, \vec{r}')$, is given by

$$S(f, \vec{r}') = \sqrt{\frac{k}{8\pi}} e^{-ik\pi/4} \int_{\Sigma} S(f, \vec{r}) e^{ik|\vec{r}' - \vec{r}|} (\hat{n}_1 + \hat{n}_2) \hat{n} dl \quad (1)$$

where Σ is a closed loop on the surface of the finite difference grid, $s(f, \vec{r})$ is the Rayleigh wavefield at location \vec{r} on the loop Σ , \vec{r}' is the receiver location, $k = \omega/c$, c is the far-field phase velocity, \hat{n}_1 is the normal vector from \vec{r} to \vec{r}' , \hat{n}_2 is the propagation direction of the Rayleigh wavefield at location \vec{r} , and \hat{n} is the normal of Σ at location \vec{r} .

It should be noted that for any teleseismic path, additional heterogeneity will further focus/defocus the surface waves. The hybrid Fresnel-Kirchoff finite difference (FK-FD) method only models near-source scattering as it would be seen in an otherwise homogeneous structure outside the finite difference model.

The predicted FK-FD far-field Rayleigh wave amplitudes in several bandwidths are shown in Figure 19a and b assuming a phase velocity range of 3.5 to 3.7 km/s. The effect of selecting the phase velocity to propagate Rayleigh waves away from the finite difference grid is addressed in Figure 19c and shows that a significant variation in assumed phase velocity has little effect on the apparent radiation pattern.

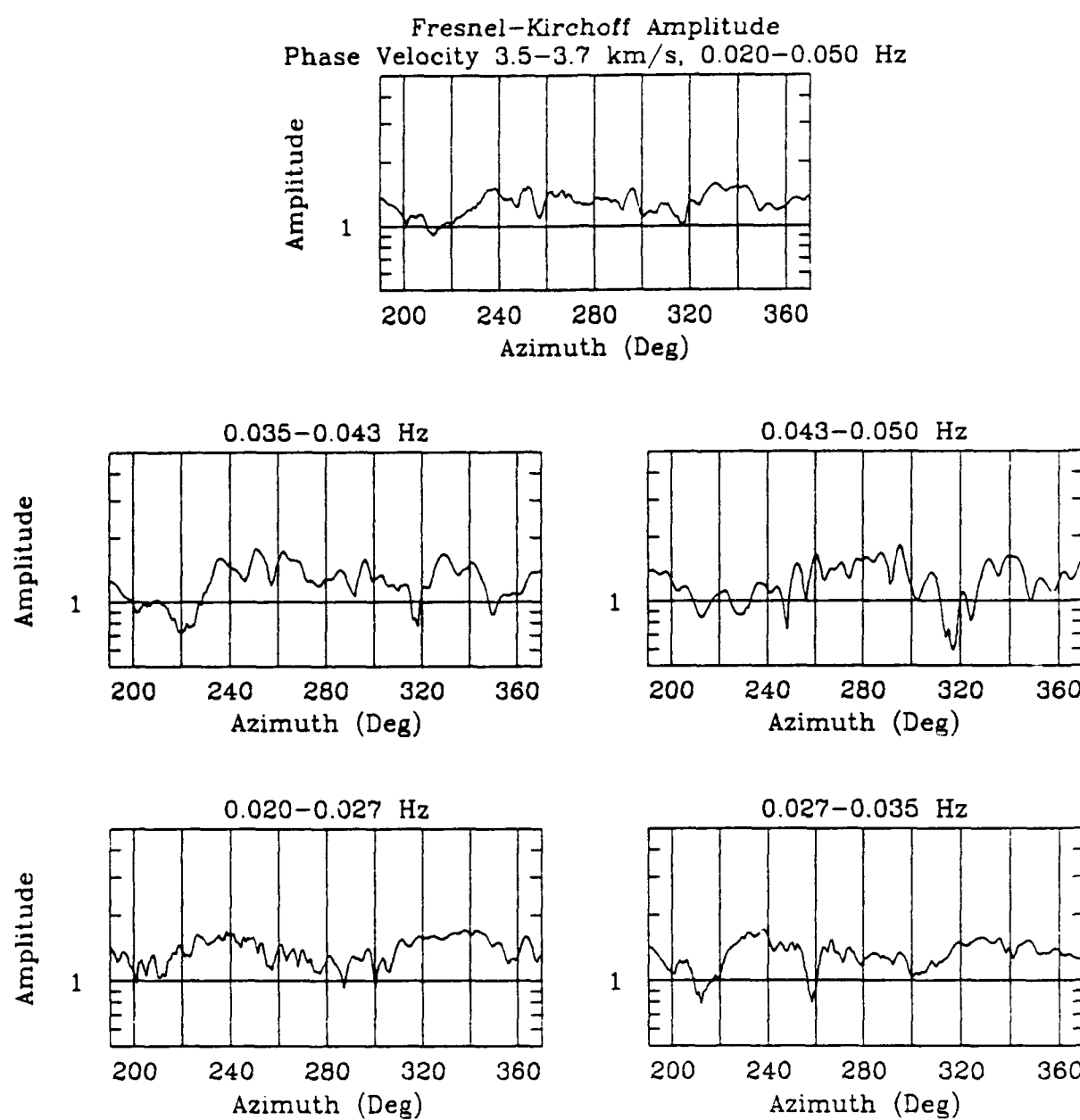
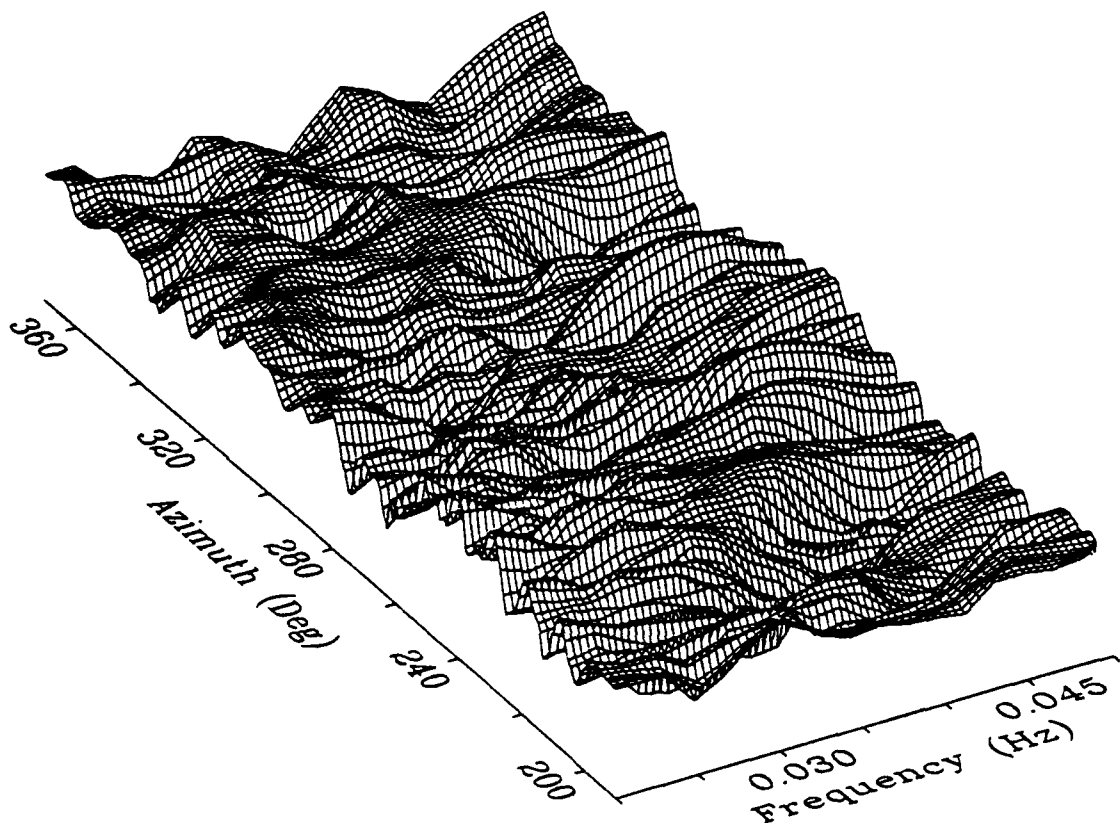


Figure 19a. Predicted Fresnel-Kirchoff amplitudes for teleseismic Rayleigh waves in several bandwidths. Note the smaller overall variation in amplitudes at lower frequencies (0.020–0.027 Hz) versus the higher frequencies (0.043–0.050 Hz). The average amplitudes (TOP) over the widest bandwidth (0.020–0.050 Hz) have the least variation as a function of azimuth from the source.

Fresnel-Kirchoff Log-Amplitudes



Phase Velocity 3.5–3.7 km/s; min = -1.6, max = 1.6

Figure 19b Perspective mesh of the predicted Fresnel-Kirchoff amplitudes for teieseismic Rayleigh waves as a function azimuth from the source (190-370 degrees) and frequency (0.02-0.05 Hz). Note the greater variation in the apparent radiation pattern at high frequencies.

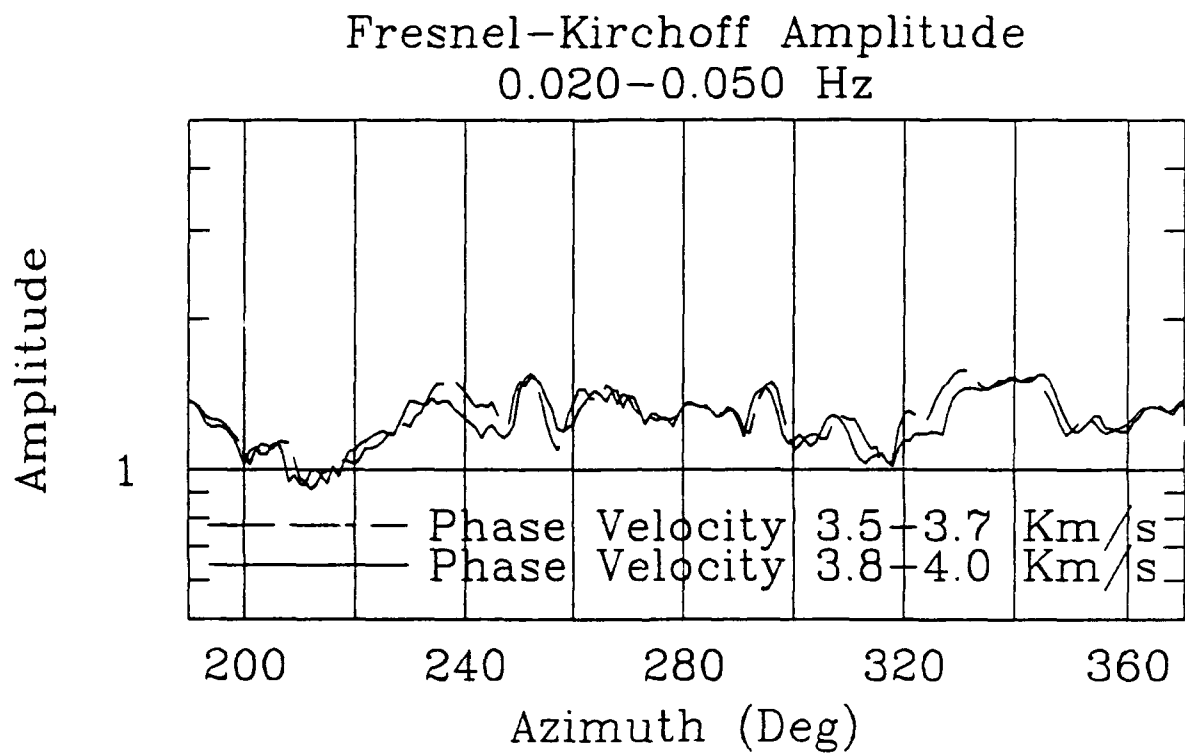


Figure 19c. Predicted Fresnel-Kirchoff amplitudes for 0.02-0.05 Hz teleseismic Rayleigh waves assuming two ranges in phase velocity, 3.5-3.7 and 3.8-4.0 km/s. The apparent radiation pattern is insensitive to the assumed far-field phase velocity used in the Fresnel-Kirchoff integral.

The FK-FD method predicts localized anomalies in amplitude of as much as 50% over azimuthal ranges of several degrees. Averaged over all azimuths the rms variation ranges from 0.05 to 0.1 rms log-amplitude depending upon the frequency bandwidth of interest. Note the smaller overall variation in amplitudes at lower frequencies (0.020-0.027 Hz) versus the higher frequencies (0.043-0.050 Hz). Amplitudes averaged over the largest bandwidth (0.020 to 0.050 Hz) have reduced variation compared to the any sub-bandwidth.

The high- and low-frequency surface waves are affected differently by the laterally varying structure and are focused/defocused at different azimuths. For source size estimation, averaging over the widest possible bandwidth may be desirable to reduce near-source focusing-defocusing effects. Furthermore, given the greater variability of the apparent radiation pattern at high frequencies (Figure 19b) it may be desirable to apply a frequency dependent weighting to Rayleigh wave amplitudes.

8. CONCLUSIONS AND DISCUSSION

A 3D geo-tectonic model based on review of seismic, gravity, and magnetic surveys was used to construct a 3D computational velocity and density model for a 3D finite difference simulation. The calculation was designed to simulate 20 to 50 second waves from an isotropic explosion source in a 3D heterogeneous structure 1620 by 1620 by 210 km. Although 2D finite difference simulations are becoming commonplace in seismological investigations, 3D computations are just beginning to be useful. Such calculations can be considered to scale with size and bandwidth, so a similar calculation could be performed in the 0.4 to 1 Hz bandwidth for a structure 81 by 81 by 21 km. Care must be exercised in choosing the target bandwidth and designing the grid. However, only a 3D finite difference calculation is capable of simulating the complexity of wave propagation phenomena that was exhibited in this calculation. Refraction, focusing-defocusing, and wave conversion were observed to result as waves were scattered by heterogeneities with characteristic sizes comparable to the wavelengths of interest.

Focusing-defocusing is observed from 0.02 to 0.05 Hz and shows considerable dependence upon frequency. While the 0.05 Hz surface waves are strongly affected by the low velocity basins, the 0.02 Hz waves see compensating effects of a shallower Moho and are refracted differently. These compensating effects suggest that focusing-defocusing should not be considered a broadband effect and averaging over the widest possible bandwidth is desirable. Furthermore, since focusing-defocusing of surface waves is most variable at shorter wavelengths, a frequency dependent weighting may be appropriate for source size estimation.

Although there is ample opportunity for teleseismic surface waves to be further refracted outside the near-source region the Fresnel-Kirchoff far-field amplitudes suggest that near-source scattering may be responsible for about 0.1 rms log-amplitude variation in narrow bandwidths and about 0.06 rms log-amplitude scatter in the 0.05 to 0.02 Hz bandwidth. This compares with 0.2 rms log-amplitude scatter observed in station corrections from the northern Novaya Zemlya test site or about 25% of the total variance. From our variogram analysis of the station corrections we concluded that about 30% of the variance in the

station effects was correlated over narrow azimuthal ranges. This is consistent with the simulation results that predict rapid variations in teleseismic amplitude with azimuth.

It should also be noted that estimation of attenuation by spectral slope can be disturbed by frequency dependent focusing-defocusing of teleseismic surface waves. For example, some azimuths would appear as low Q where the 0.02 Hz waves are focused and the 0.05 Hz waves are defocused. At other azimuths the reverse can happen with the result that the path appears as high Q. Focusing-defocusing effects may therefore contribute to uncertainties in attenuation path corrections and further contribute to the scatter in station corrections.

Evidence of surface wave multipathing was evident in the 3D simulation as surface waves found faster paths around low velocity basins in the model. This supports the multipath observations by Levshin and Berteussen (1979) of NORSAR recordings from Novaya Zemlya explosions. However, the simulations suggest that these multipaths are refracted arrivals rather than reflections from structural features as suggested by Levshin and Berteussen. No surface wave reflections were clearly apparent in the simulations despite sharp structural discontinuities in the velocity model. Refracted and converted energy clearly dominates the scattered wavefield.

Rayleigh to Love wave conversion was observed in the simulation. Conversion is most intense in regions where Rayleigh waves are obliquely incident upon structural boundaries. These regions were most clearly seen where the wavefront curvature was greatest across a fast-to-slow structural boundary. The Love waves were then observed to propagate independently of the Rayleigh waves. In localized regions of the grid, transverse to radial component ratios exceed 1/4 at 0.04 Hz and 1/2 at 0.025 Hz. Frequency wavenumber processing confirms that Love wave type motion is propagating in the grid away from the source region. As in a related study (McLaughlin, et al., 1991) of propagation in a 3D subduction zone structure, the simulations predict that teleseismic Love waves should be observed in narrow isolated azimuthal ranges. It is quite possible that such weak Love waves observed on a sparse network could be interpreted as Love waves from tectonic release.

9. ACKNOWLEDGEMENTS

The 3D finite difference calculations conducted on the Phillips Laboratory CRAY-2 were made possible by Mr. J. Lewkowicz and Ms. J. McPhetres of Phillips Laboratory LWH. This work was monitored by AFTAC under contract F08606-89-C-0022.

10. REFERENCES

Azbel, I. Y., A. F. Buyanov, V. T. Ionkis, N. V. Sharov, and V. P. Sharova (1989). Crustal Structure of the Kola Peninsula from inversion of deep seismic sounding data, *Tectonophysics*, 162, 87-99.

Burger, R. W., T. Lay, T. C. Wallace and L. J. Burdick (1986), "Evidence of Tectonic Release in Long-Period S-Waves from Underground Nuclear Explosions at the Novaya Zemlya Test Sites," *Bull. Seism. Soc. Am.*, 76, 733-755.

Chan, W. W., and B. J. Mitchell (1985). Surface-wave dispersion, crustal structure, and sediment thickness variations across the Barents Shelf, *Geophys. J. R. astr. Soc.* 80, 329-344.

Clarke, J. W. and J. Rachlin (1990). Geology of the Barents Sea Structural Basin, draft of USGS Open File Report.

Levshin, A., and K. A. Berteussen (1979). Anomalous propagation of surface waves in the Barents Sea as inferred from NORSAR recordings, *Geophys. J. R. astr. Soc.* 56, 97-118.

McLaughlin, K. L., T. G. Barker, S. M. Day, B. Shkoller, and J. L. Stevens (1991). Effects of Subduction Zone Structure on the Propagation of Explosion-Generated Long-Period Rayleigh Waves, submitted to *Geophysical Journal International*.

Stevens, J. L. (1986). Estimation of scalar moments from explosion-generated surface waves, *Bull. Seism. Soc. Am.*, 76, 123-151.

Stevens, J. L. and K. L. McLaughlin (1989). Analysis of surface waves from the Novaya Zemlya, Mururoa, and Amchitka test sites, and maximum likelihood estimation of scalar moments from earthquakes and explosions, SSS-TR-89-9953, S-CUBED, La Jolla, CA. 92038.

Tucker, W. C., G. R. Mellman and J. W. Given (1989), "Using Long-Period Surface Waves to Estimate the Isotropic Moment of Underground Explosions at Novaya Zemlya," Technical Report SGI-R-89-141, Sierra Geophysics, Kirkland, WA.

Tucker, W. C., G. R. Mellman, and M. Henry (1990). Estimation of explosion moments at Mururoa, and tectonic release orientation at Novaya Zemlya, SGI-R-90-143, Sierra Geophysics, Kirkland, WA. 98033.

Zeng, Y., T-L. Teng, and K. Aki (1989). Surface wave ray tracing and Ms:Yield determination in a laterally heterogeneous Earth, AFGL-TR-89-0065, University of Southern California, CA. 90060.

DISTRIBUTION LIST
FOR UNCLASSIFIED REPORTS
DARPA-FUNDED PROJECTS
(Last Revised: 24 Feb 92)

<u>RECIPIENT</u>	<u>NUMBER OF COPIES</u>
DEPARTMENT OF DEFENSE	
DARPA/NMRO ATTN: Dr R. Alewine 3701 N. Fairfax Drive Arlington VA 22203-1714	1
Defense Intelligence Agency Directorate for Scientific and Technical Intelligence Washington DC 20340-6160	1
Defense Nuclear Agency Shock Physics Directorate/SD Washington DC 20305-1000	1
Defense Technical Information Center Cameron Station Alexandria VA 22314	2
DEPARTMENT OF THE AIR FORCE	
AFOSR/NP Bldg 410, Room C222 Bolling AFB Washington DC 20332-6448	1
AFTAC/STINFO Patrick AFB FL 32925-6001	1
AFTAC/TT Patrick AFB FL 32925-6001	3
AFWL/NTESG Kirtland AFB NM 87117-6008	1
PL/GPEH ATTN: Mr James Lewkowicz Earth Sciences Division Hanscom AFB MA 01731-5000	1

DEPARTMENT OF THE NAVY

NORDA
ATTN: Dr J.A. Ballard
Code 543
NSTL Station MS 39529

1

DEPARTMENT OF ENERGY

Department of Energy
ATTN: Mr Max A. Koontz (DP-5.1, 4B041)
PO Box 23865
Washington DC 20024

1

Lawrence Livermore National Laboratory
ATTN: Dr J. Hannon, Dr S. Taylor, and Dr K. Nakanishi
University of California
PO Box 808
Livermore CA 94550

3

Los Alamos Scientific Laboratory
ATTN: Dr C. Newton
PO Box 1663
Los Alamos NM 87544

2

Sandia National Laboratories
ATTN: Mr P. Stokes, Dept 9110
PO Box 5800
Albuquerque NM 87185

1

OTHER GOVERNMENT AGENCIES

Central Intelligence Agency
ATTN: Dr L. Turnbull
OSI/NED, Room 5P0130
Washington DC 20505

1

US Arms Control and Disarmament Agency
ATTN: Dr M. Eimer
Verification and Intelligence Bureau, Rm 5741
Washington DC 20451

1

US Arms Control and Disarmament Agency
ATTN: Mr R.J. Morrow
320 21st Street NW
Washington DC 20451

1

US Geological Survey
ATTN: Dr T. Hanks
National Earthquake Research Center
345 Middlefield Road
Menlo Park CA 94025

1

OTHER GOVERNMENT AGENCIES (continued)

US Geological Survey MS-913
ATTN: Dr R. Masse
Global Seismology Branch
Box 25046, Stop 967
Denver Federal Center
Denver CO 80225

1

UNIVERSITIES

Boston College
ATTN: Dr A. Kafka
Western Observatory
381 Concord Road
Weston MA 02193

1

California Institute of Technology
ATTN: Dr D. Harkrider
Division of Geological and Planetary Sciences
Seismological Laboratory
Pasadena CA 91125

1

Columbia University
ATTN: Dr L. Sykes
Lamont-Doherty Geological Observatory
Palisades NY 10964

1

Cornell University
ATTN: Dr M. Barazangi
INSTOC
3126 Snee Hall
Ithaca NY 14853

1

Harvard University
ATTN: Dr J. Woodhouse
Hoffman Laboratory
20 Oxford Street
Cambridge MA 02138

1

Massachusetts Institute of Technology
ATTN: Dr S. Soloman, Dr N. Toksoz, and Dr T. Jordan
Earth Resources Laboratory
42 Carleton Street, E34-440
Cambridge MA 02142

3

Southern Methodist University
ATTN: Dr E. Herrin and Dr B. Stump
Geophysical Laboratory
Dallas TX 75275

2

UNIVERSITIES (continued)

State University of New York at Binghamton ATTN: Dr F. Wu Department of Geological Sciences Binghamton NY 13902-6000	1
St Louis University ATTN: Dr B. Mitchell and Dr R. Herrmann Department of Earth and Atmospheric Sciences 3507 Laclede St. Louis MO 63156	2
Pennsylvania State University, The ATTN: Dr S. Alexander Geosciences Department 537 Deike Building University Park PA 16802	1
University of Arizona ATTN: Dr T. Wallace Department of Geosciences, Bldg 77 Tucson AZ 85721	1
University of California, Berkeley ATTN: Dr T. McEvilly Department of Geology and Geophysics Berkeley CA 94720	1
University of California, Los Angeles ATTN: Dr L. Knopoff 405 Hilgard Avenue Los Angeles CA 90024	1
University of California, San Diego ATTN: Dr J. Orcutt Scripps Institute of Oceanography, IGPP, A-025 La Jolla CA 92093	1
University of California, Santa Cruz ATTN: Dr T. Lay Earth Sciences Board, Institute of Tectonics Santa Cruz CA 95064	1
University of Colorado ATTN: Dr C. Archambeau CIRE, Campus Box 449 Boulder CO 80309	1
University of Illinois ATTN: Dr S. Grand Department of Geology 1301 West Green Street Urbana IL 61801	1

UNIVERSITIES (continued)

University of Southern California 1
ATTN: Dr K. Aki
Center for Earth Sciences
University Park
Los Angeles CA 90089-0741

DEPARTMENT OF DEFENSE CONTRACTORS

Analytical Sciences Corporation, The 1
ATTN: Document Control (Dr Richard Sailor)
55 Walkers Brook Drive
Reading MA 01867

Applied Theory, Inc. 1
ATTN: Dr J. Trulio
930 South La Brea Avenue, Suite 2
Los Angeles CA 90036

Center for Seismic Studies 2
ATTN: AFTAC Representative
1300 N. 17th Street, Suite 1450
Arlington VA 22209

ENSCO, Inc. 1
ATTN: Mr John R. Stevenson
PO Box 1346
Springfield VA 22151

ENSCO, Inc. 1
ATTN: Dr R. Kemerait
445 Pineda Court
Melbourne FL 32940-7508

Gould, Inc. 1
ATTN: Mr R.J. Woodard
Chesapeake Instrument Division
6711 Baymeado Drive
Glen Burnie MD 21061

Maxwell Laboratories, Inc. 1
S-CUBED Reston Geophysics Office
Reston International Center
ATTN: Mr J. Murphy, Suite 1212
11800 Sunrise Valley Drive
Reston VA 22091

Pacific Sierra Research Corp. 1
ATTN: Mr F. Thomas
12340 Santa Monica Boulevard
Los Angeles CA 90025

DEPARTMENT OF DEFENSE CONTRACTORS (Continued)

Rockwell International ATTN: B. Tittmann 1049 Camino Dos Rios Thousand Oaks CA 91360	1
Rondout Associates, Inc. ATTN: Dr P. Pomeroy PO Box 224 Stone Ridge NY 12484	1
Science Applications International Corporation ATTN: Document Control (Dr T. Bache, Jr.) 10210 Campus Point Drive San Diego CA 92121	1
Science Horizons ATTN: Dr T. Cherry and Dr J. Minster 710 Encinitas Blvd, Suite 101 Encinitas CA 92024	2
S-CUBED, A Division of Maxwell Laboratories, Inc ATTN: Dr Keith L. McLaughlin PO Box 1620 La Jolla CA 92038-1620	1
Sierra Geophysics, Inc. ATTN: Dr R. Hart and Dr G. Mellman 11255 Kirkland Way Kirkland WA 98033	2
SRI International ATTN: Dr A. Florence 333 Ravensworth Avenue Menlo Park CA 94025	1
Teledyne Industries, Inc. Teledyne Geotech Alexandria Laboratories ATTN: Mr W. Rivers 314 Montgomery Street Alexandria VA 22314-1581	1
Woodward-Clyde Consultants ATTN: Dr L. Burdick PO Box 93254 Pasadena CA 91109-3254	1

NON-US RECIPIENTS

Ministry of Defense ATTN: Mr Peter Marshall Blacknest, Brimpton Reading, RG7-4RS United Kingdom	1
National Defense Research Institute ATTN: Dr Ola Dahlman Stockholm 80 Sweden	1
NTNF/NORSAR ATTN: Dr Frode Ringdal PO Box 51 N-2007 Kjeller Norway	1
University of Cambridge, Bullard Laboratories ATTN: Dr Keith Priestley Department of Earth Sciences Madingley Rise, Madingley Road Cambridge, CB3 0EZ United Kingdom	1

OTHER DISTRIBUTION

To be determined by the project office	9
--	---

TOTAL 80